The Astrophysical Journal, 668:45–61, 2007 October 10

SPITZER MID- TO FAR-INFRARED FLUX DENSITIES OF DISTANT GALAXIES[1]

Casey Papovich,[2,3] Gregory Rudnick,[4] Emeric Le Floc'h,[2,3,5] Pieter G. van Dokkum,[6] George H. Rieke,[2]
Edward N. Taylor,[7] Lee Armus,[8] Eric Gawiser,[6] Jiasheng Huang,[9]
Delphine Marcillac,[2] and Marijn Franx[7]
Received 2007 February 19; accepted 2007 June 20

ABSTRACT

We study the infrared (IR) properties of high-redshift galaxies using deep *Spitzer* 24, 70, and 160 μm data. Our primary interest is to improve the constraints on the total IR luminosities, $L_{\rm IR}$, of these galaxies. We combine the *Spitzer* data in the southern Extended Chandra Deep Field with a K_s-band–selected galaxy sample and photometric redshifts from the Multiwavelength Survey by Yale-Chile. We used a stacking analysis to measure the average 70 and 160 μm flux densities of $1.5 < z < 2.5$ galaxies as a function of 24 μm flux density, X-ray activity, and rest-frame near-IR color. Galaxies with $1.5 < z < 2.5$ and $S_{24} = 53$–250 μJy have $L_{\rm IR}$ derived from their average 24–160 μm flux densities within factors of 2–3 of those inferred from the 24 μm flux densities only. However, $L_{\rm IR}$ derived from the average 24–160 μm flux densities for galaxies with $S_{24} > 250$ μJy and $1.5 < z < 2.5$ are lower than those inferred using only the 24 μm flux density by factors of 2–10. Galaxies with $S_{24} > 250$ μJy have S_{70}/S_{24} flux ratios comparable to sources with X-ray detections or red rest-frame IR colors, suggesting that warm dust possibly heated by AGNs may contribute to the high 24 μm emission. Based on the average 24–160 μm flux densities, nearly all 24 μm–selected galaxies at $1.5 < z < 2.5$ have $L_{\rm IR} < 6 \times 10^{12}$ $L_\odot$, which, if attributed to star formation, corresponds to $\Psi < 1000$ $M_\odot$ yr^{-1}. This suggests that high-redshift galaxies may have star formation efficiencies and feedback processes similar to those of local analogs. Objects with $L_{\rm IR} > 6 \times 10^{12}$ $L_\odot$ are quite rare, with a surface density $\sim 30 \pm 10$ deg^{-2}, corresponding to $\sim 2 \pm 1 \times 10^{-6}$ Mpc^{-3} over $1.5 < z < 2.5$.

Subject headings: galaxies: high-redshift — infrared: galaxies

1. INTRODUCTION

Observations with *ISO*, SCUBA, and more recently the *Spitzer Space Telescope* show that high-redshift galaxies contain large amounts of dust, which emit strongly at infrared (IR) wavelengths. Although locally, IR-luminous galaxies are rather rare (e.g., Soifer et al. 1987; Soifer & Neugebauer 1991), number counts from *ISO* and *Spitzer* demonstrate that this population evolves very rapidly (Elbaz et al. 1999; Papovich et al. 2004), dominating the star formation rate (SFR) density and cosmic IR background by $z \sim 1$ (e.g., Franceschini et al. 2001; Elbaz et al. 2002; Le Floc'h et al. 2005; Pérez-González et al. 2005; Dole et al. 2006). Recent observations from the Multiband Imaging Photometer for *Spitzer* (MIPS; Rieke et al. 2004) are sensitive to the IR emission from galaxies at yet higher redshifts. Several studies using *Spitzer* 24 μm observations demonstrated that at $1.5 \lesssim z \lesssim 3$ the density of ultraluminous IR galaxies (ULIRGs) with $L(8\text{–}1000\ \mu\text{m}) > 10^{12}$ $L_\odot$ was $\approx$1000 times higher than at present (Daddi et al. 2005; Papovich et al. 2006), and that $\sim$50% of massive galaxies (stellar masses $M \gtrsim 10^{11}$ $M_\odot$) at these redshifts emit strongly at 24 μm (Daddi et al. 2005; Caputi et al. 2006; Papovich et al. 2006; Reddy et al. 2006; Webb et al. 2006). Thus, more than half of the massive galaxies at $z \sim 2$ are either actively forming stars, fueling supermassive black holes, or both.

The high incidence of IR-active, massive galaxies at $1.5 \lesssim z \lesssim 3$ coincides with rapid evolution in the stellar mass density. Most ($\gtrsim$50%) of the stellar mass in galaxies today formed during the short time between $z \sim 3$ and 1 (Dickinson et al. 2003; Rudnick et al. 2003, 2006; Fontana et al. 2003, 2004; Glazebrook et al. 2004). Much of this stellar mass density resides in massive galaxies, which appear at epochs prior to $z \sim 1$–2 (see McCarthy 2004; Renzini 2006 for reviews). This is consistent with recent theoretical work by, for example, De Lucia et al. (2006), who argue that most of the star formation in massive galaxies occurs at early look-back times.

The *Spitzer* IR observations of high-redshift galaxies may be revealing vigorous star formation episodes. However, to date, most studies rely on converting the 24 μm flux densities from *Spitzer* to total IR luminosities, $L_{\rm IR} \equiv L(8\text{–}1000\ \mu\text{m})$, and then to the instantaneous SFR (e.g., Kennicutt 1998). At $z \sim 2$ the 24 μm band probes rest-frame 8 μm. While this wavelength broadly correlates with $L_{\rm IR}$, there may be large variations with bolometric luminosity and galaxy type (e.g., Chary & Elbaz 2001; Roussel et al. 2001; Elbaz et al. 2002; Calzetti et al. 2005, 2007; Alonso-Herrero et al. 2006a; Brandl et al. 2006), and significant scatter may be expected because of the range of shapes of the IR spectral energy distributions (SEDs) (e.g., Dale et al. 2001, 2005; Papovich & Bell 2002; Armus et al. 2007).

Broadly, there are few constraints on the relation between the observed 24 μm (rest-frame 8 μm) and the total bolometric emission for $z \sim 2$ galaxies. Daddi et al. (2005) found that the average (stacked) X-ray, UV, mid-IR, submillimeter, and radio emission of *BzK*-selected star-forming galaxies at $1.4 < z < 2.5$ gave consistent estimates for the instantaneous SFR. Egami et al.

[1] This work is based in part on observations made with the *Spitzer Space Telescope*, which is operated by the Jet Propulsion laboratory, California Institute of Technology, under NASA contract 1407.

[2] Steward Observatory, University of Arizona, Tucson, AZ 85721; papovich@as.arizona.edu.
[3] Spitzer Fellow.
[4] Goldberg Fellow, National Optical Astronomy Observatories, Tucson, AZ 85721.
[5] Current address: Institute for Astronomy, University of Hawaii, Honolulu, HI 96822.
[6] Department of Astronomy and Yale Center for Astronomy and Astrophysics, Yale University, New Haven, CT 06520.
[7] Leiden Observatory, Leiden University, 2300 RA Leiden, Netherlands.
[8] *Spitzer* Space Center, California Institute of Technology, Pasadena, CA, 91125.
[9] Harvard-Smithsonian Center for Astrophysics, Cambridge, MA 02138.

(2004) and Pope et al. (2006) showed that the 24 μm emission from $z \sim 2$–3 submillimeter-selected objects provided an accurate measure of the total bolometric emission for galaxies relative to that inferred from the combined 24 μm, 850 μm, and 1.4 GHz radio data. Although *on average* 24 μm observations of $z \sim 2$ provide an accurate measure of the total IR luminosity (at the factor of 2 level), one must exercise care when using 24 μm data as a total IR indicator at high redshifts as the conversion between the mid-IR and total IR have not yet converged (e.g., Papovich & Bell 2002; Armus et al. 2007; Daddi et al. 2007a), and individual estimates may have large errors.

Observations at wavelengths longer than 24 μm are required to improve our constraints on the shape of the IR SED in distant galaxies. At redshifts $z = 2$ the *Spitzer* 70 and 160 μm bands probe rest-frame 24 and 55 μm, respectively. The rest-frame 24 μm emission, in particular, correlates strongly with the total IR luminosity and SFR with substantially smaller scatter than the luminosity at rest-frame 8 μm for star-forming regions and starburst galaxies (Calzetti et al. 2005; Alonso-Herrero et al. 2006a; but see Calzetti et al. 2007). As discussed in Papovich & Bell (2002), the S_{70}/S_{24} ratio better correlates with the total far-IR emission at these redshifts, providing tight constraints on the total far-IR emission to <30%. Furthermore, Siebenmorgen & Krügel (2007) showed that fitting their theoretical models for the IR emission from galaxies to the rest-frame 8 and 24 μm flux densities provided a tight constraint on the shape of the IR SED and total IR luminosity.

In this paper we study the IR properties of high-redshift galaxies using deep *Spitzer* 24, 70, and 160 μm data. Our primary interest is to improve our constraints on the total IR luminosities from high-redshift galaxies detected at 24 μm using the longer wavelength MIPS data. However, 70 and 160 μm observations detect few galaxies directly at $z \gtrsim 1$ (e.g., Frayer et al. 2006a, 2006b; Huynh et al. 2007; Daddi et al. 2007a) owing primarily to the larger angular resolution and poorer sensitivity of *Spitzer* at 70 and 160 μm relative to 24 μm. Therefore, we use stacking methods to study the average 70 and 160 μm flux densities of galaxies. Here, we study a large sample of galaxies with $1.5 < z < 2.5$, which allows us to measure the average 70 and 160 μm flux densities of subpopulations of galaxies, divided as a function of 24 μm flux density, and for galaxies with putative AGNs inferred from X-ray activity or red rest-frame near-IR colors. Thus, we study the IR properties of distant galaxies during the epoch where a substantial fraction of massive galaxies are in active IR phases of their evolution.

Throughout this work we quote optical and near-IR magnitudes on the AB system where $m_{\rm AB} = 23.9 - 2.5 \log (f_\nu/1\ \mu{\rm Jy})$ unless otherwise specified. We denote magnitudes measured from the data with *Spitzer* IRAC in the four channels [3.6], [4.5], [5.8], and [8.0], respectively. Similarly, we denote the flux density, f_ν, in the MIPS 24, 70, and 160 μm bands as S_{24}, S_{70}, and S_{160}, respectively. To derive rest-frame quantities, we use a cosmology with $\Omega_m = 0.3$, $\Lambda = 0.7$, and $H_0 = 70$ km s^{-1} Mpc^{-1}.

2. DATA

For this study, we used data in the Extended *Chandra* Deep Field South (ECDF-S), which has field center coordinates $3^{\rm h}32^{\rm m}30^{\rm s}$, $-27^\circ48'20''$. The ECDF-S has been targeted by a large array of ground-based and space-based telescopes, and it has deep multiwavelength coverage. For this study, we make use of data sets covering a large area (775 arcmin^2) in the ECDF-S from the Multiwavelength Survey by Yale-Chile (MUSYC), the *Spitzer Space Telescope*, and the *Chandra X-Ray Observatory*.

TABLE 1
Flux Completeness and Accuracy of the ECDF-S *Spitzer* MIPS Data

Band (μm)	$\langle t_{\rm exp}\rangle$ (s)	C(50%)	C(80%)	$\langle f_\nu({\rm S/N}=3)\rangle$	$\langle f_\nu({\rm S/N}=5)\rangle$
24.....	2700	51	71	53	110
70.....	1100	3.9	6.6	4.6	8.2
160.....	300	20	44	24	59

Note.—Units of flux density are μJy for 24 μm and mJy for 70 and 160 μm.

2.1. *MUSYC*

The MUSYC data include *UBVRIzJHK*$_s$ imaging in a $31' \times 31'$ field in the ECDF-S. Gawiser et al. (2006) discuss the observations, images, and data reduction of the *U*- through *z*-band images. E. Taylor et al. (2007, in preparation) describe the details of the *JHK*$_s$ observations and data reduction, and of the source detection and cataloging processes. In summary, we performed object detection and photometry on images convolved to match the image quality of the image with the poorest seeing to account for seeing variations. Objects were detected in the K_s-band data using the SExtractor software (Bertin & Arnouts 1996), and colors were measured in 2.25″ diameter apertures (SExtractor MAG_APER magnitudes) on the seeing-matched images in each band. We scaled the aperture magnitudes to total magnitudes using the difference between the K_s-band aperture (MAG_APER) and total (MAG_AUTO) apertures, $\Delta m = {\rm MAG\_APER}(K_s) - {\rm MAG\_AUTO}(K_s)$. The catalog reaches a 5 σ sensitivity of $K_s = 22.2$ mag (E. Taylor et al. 2007, in preparation)

2.2. *Spitzer*

The *Spitzer* Guaranteed Time Observers (GTOs) observed the ECDF-S with both the IRAC and MIPS instruments, covering 3–160 μm. IRAC data covers 3–8 μm in four bands centered at 3.6, 4.5, 5.8, and 8.0 μm. We detected objects using SExtractor on the IRAC data using a weighted-summed [3.6 μm] + [4.5 μm] image. We then performed photometry using SExtractor in circular apertures of diameter 4″, and converted these to total magnitudes by applying aperture corrections derived from the measured point-source curve of growth of 0.30, 0.34, 0.53, and 0.67 mag to the [3.6 μm], [4.5 μm], [5.8 μm], and [8.0 μm] photometry, respectively. To estimate the photometric uncertainties we repeatedly added artificial sources to the IRAC data, and reperformed object detection and photometry. From our analysis of these simulations the 5 σ magnitude limits for point sources are 23.3, 22.7, 21.3, and 21.6 mag in [3.6 μm], [4.5 μm], [5.8 μm], and [8.0 μm], respectively.

Papovich et al. (2004) and Dole et al. (2004) describe the data reduction and point-source photometry methods applied to the *Spitzer* MIPS 24, 70, and 160 μm images, following the procedures described in Gordon et al. (2005). Here, we use rereduced versions of the MIPS images that combine data from the original observations covering $0.5^\circ \times 1^\circ$ with a second-epoch observation, doubling the exposure time in an area $\approx 0.5^\circ \times 0.5^\circ$ centered on the ECDF-S field. Table 1 gives the average exposure time for MIPS in the combined observations. The second-epoch observations also reduce data artifacts, particularly in the 70 and 160 μm images. We have reanalyzed these data using the simulations described in Papovich et al. (2004) to estimate the photometric errors and source completeness in the MIPS images. Table 1 gives the 50% and 80% flux density completeness limits, C(50%) and C(80%), and the average flux densities of sources with S/N = 3

and 5 as derived from the simulations. The sample of 70 and 160 μm sources with $3 < \mathrm{S/N} < 5$ will include some spurious detections. Nevertheless, we require that these 70 and 160 μm have 24 μm counterparts, which improves the reliability of these detections and provides upper limits on S_{70}/S_{24} and S_{160}/S_{24} flux ratios.

We matched sources in the IRAC and MIPS catalogs to the MUSYC K_s-band catalog down to their approximate 3 σ limits (53, 4.6, and 24 mJy for 24, 70, and 160 μm, respectively). We used a wavelength-dependent matching radius. For IRAC, we matched sources with $r \leq 1''$ to K_s-band counterparts. Similarly for MIPS sources, we matched objects with $r \leq 1$, 4, and $16''$ to K_s-band counterparts for 24, 70, and 160 μm sources, respectively. The larger matching radii at 70 and 160 μm allow for centroid shifts owing to the lower resolution and source confusion (see, e.g., Hogg 2001). However, the larger matching radii increase the likelihood of multiple sources associated with the MIPS source. Therefore, we require that the 70 and 160 μm sources have 24 μm counterparts, improving the confidence in the associations.

2.3. *Chandra*

Two data sets with *Chandra* exist in the ECDF-S. The observations include a deep, 1 Ms, central field covering $\approx$400 arcmin^2 (Giacconi et al. 2002; Alexander et al. 2003) and a four-pointing mosaic with 250 ks depth covering $\approx$1000 arcmin^2 over the ECDF-S (Lehmer et al. 2005; Virani et al. 2006). For this study, we use both the deep *Chandra* catalogs from Alexander et al. (2003) and the shallow wide-area catalogs from Lehmer et al. (2005). The deep *Chandra* data have aim-point flux limits (S/N = 3) in the 0.5–2.0 and 2–8 keV bands of $\approx 2.5 \times 10^{-17}$ and $\approx 1.4 \times 10^{-16}$ ergs cm^{-2} s^{-1}, respectively. The shallower data over the ECDF-S have aim-point flux limits (S/N = 3) in the 0.5–2.0 and 2–8 keV bands of $\approx 1.1 \times 10^{-16}$ and $\approx 6.7 \times 10^{-16}$ ergs cm^{-2} s^{-1}, respectively. Assuming an X-ray spectral slope of $\Gamma = 2.0$, a source detected with a flux of $\approx 10^{-16}$ ergs cm^{-2} s^{-1} would have both luminosities of $\approx 5.2 \times 10^{41}$ and $\approx 7.6 \times 10^{42}$ erg s^{-1} in either the soft or hard X-ray band at $z = 1$ and $z = 3$, respectively (for this particular choice of Γ), assuming no Galactic absorption. The median positional accuracy for the sources in the *Chandra* catalogs is $0.6''$. We matched the *Chandra* sources from both the deep and shallow surveys to sources in the K_s-band catalog within $r \leq 1''$.

2.4. *Redshift Distribution of Spitzer Sources*

We used the MUSYC *UBVRIzJHK*$_s$ data to derive photometric redshifts for all objects in the K_s-band catalog, following the method of Rudnick et al. (2001, 2003). Because we are predominantly interested in the IR properties of high-redshift galaxies, we are forced to utilize photometric-redshift techniques as most massive galaxies at high redshifts are too faint for optical spectroscopic follow-up (van Dokkum et al. 2006). Here, we do not include the *Spitzer* data in the photometric redshift estimates in order to avoid uncertainties in the stellar population models that may affect the rest-frame near-IR emission (see the discussion in, e.g., Maraston et al. 2006; van der Wel et al. 2006), or possible dust emission at rest-frame wavelengths >3 μm, which is not included in the galaxy templates used for the redshift determination. A comparison between the photometric redshifts, z_{ph}, and available spectroscopic redshifts gives an accuracy of $\Delta(z)/(1+z) \simeq 0.06$ for galaxies at $z \leq 1.5$ using a biweight location estimator (see Rudnick et al. 2006). For dusty star-forming galaxies at $z > 1.5$ the accuracy is $\Delta(z)/(1+z) \simeq 0.1$, or $\Delta(z) = 0.3$ at $z = 2$. A more detailed discussion of the photometric redshifts is given elsewhere (E. Taylor et al. 2007, in preparation).

The MIPS 24, 70, and 160 μm samples matched to the MUSYC K_s-band catalog have source densities of 13,900 $\pm$ 250, 740 $\pm$ 59, and 260 $\pm$ 34 deg^{-2}, respectively, to the 3 σ limiting flux densities in Table 1. The median redshifts of the 24, 70, and 160 μm samples detected at >3 σ are $z_{\mathrm{ph,\,med}} = 0.82$, 0.44, and 0.25, respectively. Frayer et al. (2006a) report similar redshifts for MIPS 70 and 160 μm data in the *Spitzer* first look survey. Figure 1 shows the redshift distribution of the 24 and 70 μm sources matched to the K_s-band–selected sample. The matched 160 μm K_s-band list includes only 55 sources, and a histogram of their photometric redshifts yields little information in addition to the median quoted above. The shaded histogram in each panel shows the number distribution of all K_s-band sources with $K_s \leq 22.2$ mag, normalized to match the total number of MIPS sources. The hatched histograms show the MIPS redshift distributions. In each figure, the upper panel shows the χ^2_i per bin i, where $\chi^2_i = (N^i_{\mathrm{exp}} - N^i_{\mathrm{obs}})^2/N^i_{\mathrm{exp}}$, and N^i_{obs} is the number of MIPS sources per redshift bin and N^i_{exp} is the expected number if MIPS sources have the same redshift distribution as the total $K_s < 22.2$ mag population.

The redshift distribution of the 24 μm–detected galaxies is nearly identical to that expected from the K_s-band redshift distribution. Although the distributions are similar, a Kolmogorov-Smirnov test gives a low likelihood (0.1%) that the distributions have identical parent samples. Qualitatively, there are several interesting deviations. The strongest relative deficit of 24 μm sources occurs at $z \sim 0.5$. This may imply that there are relatively fewer IR-active galaxies at these redshifts in the ECDF-S, or it may result as the IR emission probed by the 24 μm band shifts from very small grains to aromatics. We also observe a relative increase in the number of 24 μm sources at $z \sim 0.7$. At this redshift the emission from strong polycyclic aromatic hydrocarbons (PAHs) at 11.3–13.5 μm shift into the 24 μm passband (e.g., Smith et al. 2007), possibly boosting the number of detected sources at this wavelength. However, we see no evidence for an increase in relative number of 24 μm sources at $1.5 < z < 2$. At these redshifts the strong PAH emission feature at 7.7 μm emission shifts into the MIPS 24 μm bandpass. This contrasts with the conclusion of Caputi et al. (2006), who find an relative excess of 24 μm sources at these redshifts in the GOODS-S field. Some of this disagreement may arise from small number statistics as the MUSYC ECDF-S field encompasses an area $\approx$6 times the size of the GOODS-S field. However, the GOODS-S data used by Caputi et al. extends to a deeper K_s-magnitude limit, and we cannot rule out that a relative excess of 24 μm sources at $1.5 < z < 2.0$ exists for fainter sources.

The redshift distribution of 70 μm sources does not generally follow the relative distribution of the total K_s-band population. Formally, a χ^2 test on the distributions shows they differ with high significance (>4 σ). Because the redshift distribution of 24 μm sources matches closely the total redshift distribution, we interpret this as evidence that the 70 μm data is not sensitive to the IR emission from most high-redshift sources. That is, at $z \gtrsim 1$ most IR-active galaxies have 70 μm flux densities $\lesssim$5 mJy. This is consistent with a study by Dye et al. (2007), who found that sources with $S_{24} > 70$ μJy and $z \sim 1$ have flux-weighted average 70 μm flux densities <2 mJy.

3. SPITZER MID-TO FAR-IR COLORS OF DISTANT GALAXIES

The MIPS flux density ratios (or "colors") of galaxies allow us to study the properties of the dust emission of high-redshift galaxies using these data. Because the data detect few 160 μm sources, we do not discuss the S_{160}/S_{24} or S_{160}/S_{70} ratios for individual sources here (see, e.g., Frayer et al. 2006a). We make

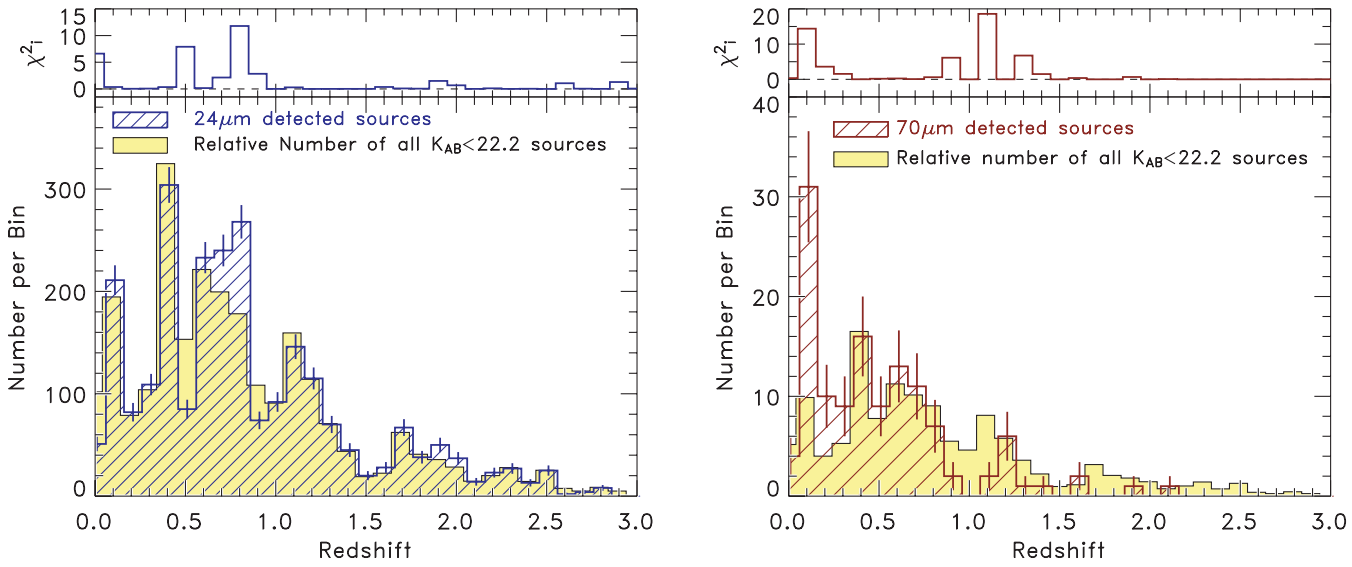

FIG. 1.—Redshift distribution of MIPS-selected galaxies in the ECDF-S field. The left panel shows the redshift distribution of 24 μm–selected galaxies with $S_{24} > 53$ μJy and $K_s < 22.2$ mag. The right panel shows the redshift distribution of 70 μm–selected galaxies with $S_{70} > 4.6$ mJy and $K_s < 22.2$ mag. The error bars show the Poissonian uncertainties on the MIPS distributions only. In both panels, the yellow, shaded region shows the relative redshift number distribution of all MUSYC sources with $K_s < 22.2$ mag, normalized to the total number of MIPS sources. The hatched regions shows the redshift number distribution of MIPS 24 and 70 μm sources (*left and right panels, respectively*). In each panel, the upper subpanel shows $\chi_i^2 = (N^i_{\rm exp} - N^i_{\rm obs})^2/N^i_{\rm exp}$ for each bin i.

further use of the 160 μm data in the analysis of the average flux densities of high-redshift galaxies in § 3.2.

3.1. *The Spitzer S_{70}/S_{24} Flux Density Ratio as a Function of Redshift*

Figure 2 shows the S_{70}/S_{24} ratios of the ECDF-S sources detected at 70 μm, compared against expectations from local-galaxy templates. At $z_{\rm ph} < 1.5$ 70 μm sources with high signal-to-noise (S/N) detections have S_{70}/S_{24} ratios within the bounds presented by the models, and range from cold-dust dominated ULIRGs such as Arp 220 to ULIRGs with "warm" mid-IR colors such as Mrk 231 (Armus et al. 2007). Several objects have S_{70}/S_{24} ratios greater than that expected from Arp 220. The most deviant of these outliers have larger uncertainties on their 24 μm flux density measurements ($3 < {\rm S/N} < 4$), reflected in their larger error bars in the figure. Several galaxies have S_{70}/S_{24} ratios lower than that of Mrk 231. However, these sources all have X-ray detections (including two that have S_{70}/S_{24} ratios consistent with constant power in νf_ν), suggesting they harbor an AGN that contributes to the mid-IR emission.

Most of the galaxies (13/15) at $1 < z_{\rm ph} < 1.5$ detected at 70 μm have high S_{70}/S_{24} ratios, but consistent with the local templates. These may have strong silicate absorption bands at ~9–10 μm (like Arp 220; see Armus et al. 2007), suppressing the 24 μm flux density and boosting the S_{70}/S_{24} ratio. The remaining 70 μm sources in this redshift range have S_{70}/S_{24} ratios consistent with star-forming galaxy templates (Dale & Helou 2002), not including one source with a S_{70}/S_{24} ratios consistent with Mrk 231, and one X-ray source discussed above.

At $1.5 < z_{\rm ph} < 2.5$, four sources are detected directly at 70 μm. All four have $S_{70}/S_{24} > 15$, consistent with the upper envelope of local ULIRG templates. However, in all cases the sources have $3 < {\rm S/N}(70\ \mu{\rm m}) < 4$. Given the relative lack of 70 μm sources at $z \gtrsim 1.5$, we reexamined the matching of the MIPS data to the MUSYC data as well as the galaxy colors ($U - K_s$ and IRAC 3–8 μm) to verify that the photometric redshifts are reasonable. (We remind the reader that the photometric redshifts use only the MUSYC optical/near-IR data.) For three of the four objects the 70 μm source matches the source in the MUSYC catalog, and the combined MUSYC and IRAC spectral energy distribution supports the assigned redshift. The remaining source lies outside the IRAC GTO coverage, but within recent *Spitzer* IRAC imaging

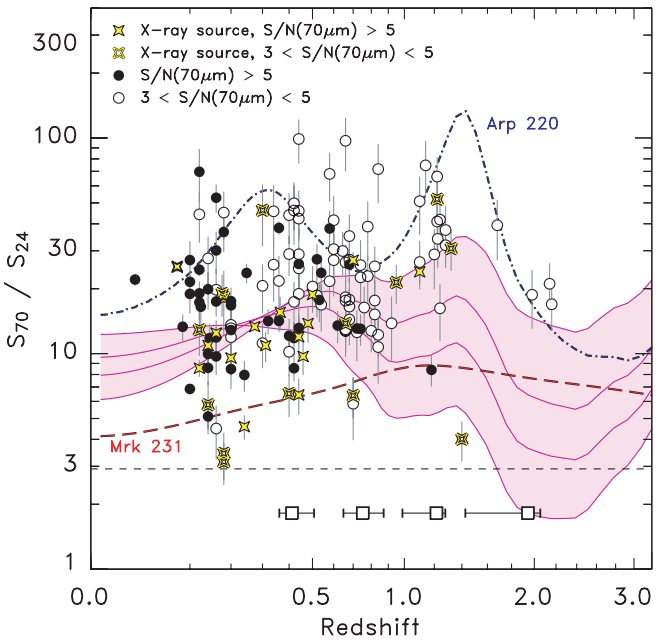

FIG. 2.—MIPS 70–24 μm flux density ratios (S_{70}/S_{24}) of galaxies detected at 70 μm in the ECDF-S as a function of redshift. Circles denote 70 μm sources without X-ray detections, while stars denote 70 μm sources with X-ray detections. Sources with ${\rm S/N}(S_{70}/S_{24}) < 3$ have been removed for clarity. The curves show expected flux density ratios of galaxy template SEDs. These include templates for the local ULIRGs Arp 220 (*blue dot-dashed line*) and Mrk 231 (*red long-dashed line*), and empirical templates from Dale & Helou (2002; *magenta-shaded region*). The horizontal short-dashed line shows the expected flux ratio for a source with constant power in νf_ν, $S_{70}/S_{24} = 2.9$. The horizontal error bars show the average uncertainty on the photometric redshifts in various redshift bins.

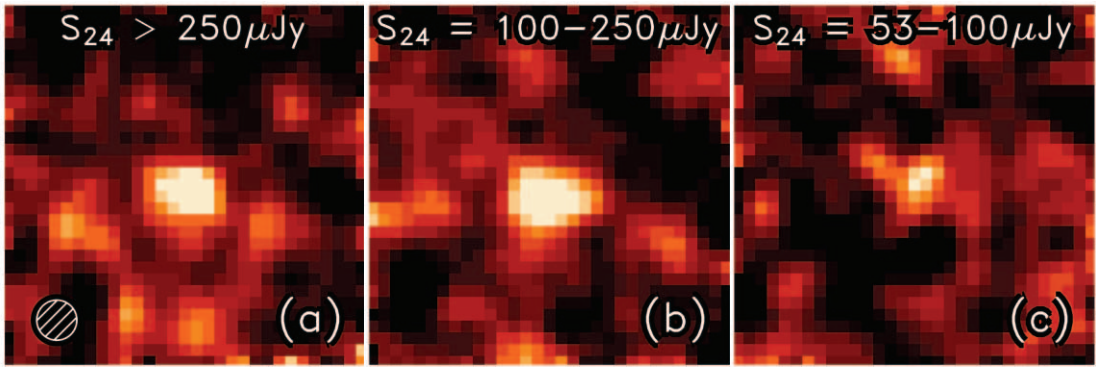

FIG. 3.—Stacked 70 μm images of ordinary IR sources at $1.5 < z_{ph} < 2.5$ (i.e., those sources without X-ray detections and IR–power-law–like colors). The panels show the stacked 70 μm emission in bins of 24 μm flux densities of (*a*) $S_{24} > 250$ μJy, (*b*) $100 \leq S_{24}/\mu\text{Jy} < 250$, (*c*) $53 < S_{24}/\mu\text{Jy} < 100$. Each panel shows a region approximately $100'' \times 100''$ (roughly 6 times the 70 μm PSF FWHM), at a scale of $4.925''$ pixel^{-1}. The filled circle, inset in panel *a*, has a diameter equal to the PSF FWHM.

(PI: P. van Dokkum). The IRAC data for this source (M. Damen 2006, private communication) supports the photometric redshift, with an SED similar to that of Arp 220, but with increased extinction in rest-frame optical and UV wavelengths. This object is also detected at 160 μm, and may be similar to the source studied by Le Floc'h et al. (2007). Regardless, the surface density of $S_{70} > 4.6$ mJy sources at $1.5 < z < 2.5$ is very low, $\Sigma \leq 19 \pm 9$ deg^{-2}.

3.2. *Average Spitzer* 70 *and* 160 μm *Flux Densities of* $1.5 < z < 2.5$ *Galaxies*

The 70 μm–detected sources at $1.5 < z < 2.5$ represent only the "brightest" galaxies at these redshifts and wavelengths. To study the typical 70 and 160 μm flux densities of all 24 μm galaxies at these redshifts, we resorted to stacking techniques to improve the effective depth of the IR data. By doing this we lose the ability to study galaxies on an object-by-object basis, but gain the ability to study the global trends on the whole. Stacking techniques have already proven valuable to study the IR emission from faint galaxies (Zheng et al. 2006, 2007) and to study the contribution of 8 μm, 24 μm, and submillimeter selected galaxies to the cosmic IR background (Dole et al. 2006; Dye et al. 2007; Huynh et al. 2007).

We selected all galaxies from the MUSYC K_s-band catalog with $S_{24} \geq 53$ μJy and $1.5 \leq z_{ph} \leq 2.5$. This sample has a mean redshift of $\langle z \rangle = 1.9$, but the distribution is skewed toward sources with lower redshift (as is evident in Fig. 1). The interquartile of the redshift distribution (including the inner 25%–75% of the distribution) spans $1.7 < z_{phot} < 2.3$.

We describe the details of our stacking method in the Appendix. Based on our simulations (described in the Appendix), we stacked sources in 70 and 160 μm images first cleaned of sources detected at >5 σ. We also excluded objects near the edge of the image and a few objects in noisy (low-weight) regions of the 70 μm image. The resulting sample includes 395 galaxies. We split this sample into bins of 24 μm flux density, $S_{24} > 250$ μJy, $100 < S_{24}/\mu\text{Jy} \leq 250$, and $53 \leq S_{24} \leq 100$ μJy. We also divide these samples into subsamples with X-ray detections (45 objects) and objects with red, rest-frame near-IR colors (76 objects, hereafter "IR–power-law" sources; see below). We hereafter denote those objects without X-ray detections or red, near-IR colors as "ordinary IR sources" (274 objects).

Even the deep X-ray data used here is insensitive to heavily obscured AGNs at $1.5 < z < 2.5$, although such objects contribute to 24 μm–selected samples. We therefore also considered a population of 24 μm sources in this redshift range with red rest-frame near-IR colors, which is indicative of the emission from warm dust at $\lambda \gtrsim 2$ μm heated by an obscured AGN (see, e.g., Lacy et al. 2004; Stern et al. 2005; Alonso-Herrero et al. 2006b; Donley et al. 2007). Following Alonso-Herrero et al. (2006b) we fit for the exponent in $f_\nu \sim \nu^\alpha$ for each 24 μm source with $1.5 < z_{ph} < 2.5$ over the IRAC bands, and selected objects with $\alpha < -0.5$ (hereafter we refer to this as the "IR–power-law" subsample). We subsequently inspected the SEDs of all the objects in this subsample visually to ensure that their IRAC colors are consistent with red power-law–like SEDs. Because power-law–selected AGNs have a high 24 μm–detection rate (e.g., Donley et al. 2007), the 24 μm selection of the IR–power-law sample increases the likelihood that they harbor AGNs. The IR–power-law sample includes 76 galaxies (including 22 X-ray sources and 54 non–X-ray sources) with $S_{24} > 53$ μJy. There is a large overlap between the subsample of X-ray sources and the IR–power-law sources—22/45 of the X-ray sources are members of the IR–power-law subsample. These two samples are not independent.

For each subsample of galaxies, we stacked the locations of each 24 μm source in the 70 and 160 μm images. We then measured the flux density in the mean image constructed from the stack. Figure 3 shows the mean of the stacked 70 μm images for the ordinary IR galaxies split into subsamples of 24 μm flux density. Figure 4 shows the stacked 160 μm images for these galaxies. Table 2 gives the measured flux densities for each of the subsamples.

In all subsamples of ordinary IR galaxies, we detect the source at 70 and 160 μm in the stacked images. We detect the X-ray and IR–power-law sources in the 70 and 160 μm images for the $S_{24} > 250$ μJy subsamples. However, we do not detect these subsamples at 70 and 160 μm in the lower flux density bins, $53 < S_{24}/\mu\text{Jy} < 100$ nor $100 < S_{24}/\mu\text{Jy} < 250$, primarily owing to the lack of objects in these subsamples. We do detect the 70 and 160 μm emission for X-ray sources and IR–power-law sources within a larger bin, $53 \leq S_{24} < 250$ μJy, and we quote these values in Table 2.

While the profile of the source in all the stacked images is consistent with the PSF and 70 and 160 μm, we observe some extra power in the wings of the stacked sources. We suspect this arises from slight astrometric offsets between the sources at 24 μm and the sources in the 70 and 160 μm images that cause a "blurring" of the source in the 70 and 160 μm stacked images. While there is no way to correct for this, we estimate that it reduces the derived flux densities by $\lesssim$10% based on differences between the observed profile and theoretical PSFs.

The choice of the flux density ranges used to delimit the subsamples in Table 2 is pragmatic, and provides sufficient numbers of objects in each bin, while minimizing the uncertainties on the stacked measurement. We have tested how changes in our flux

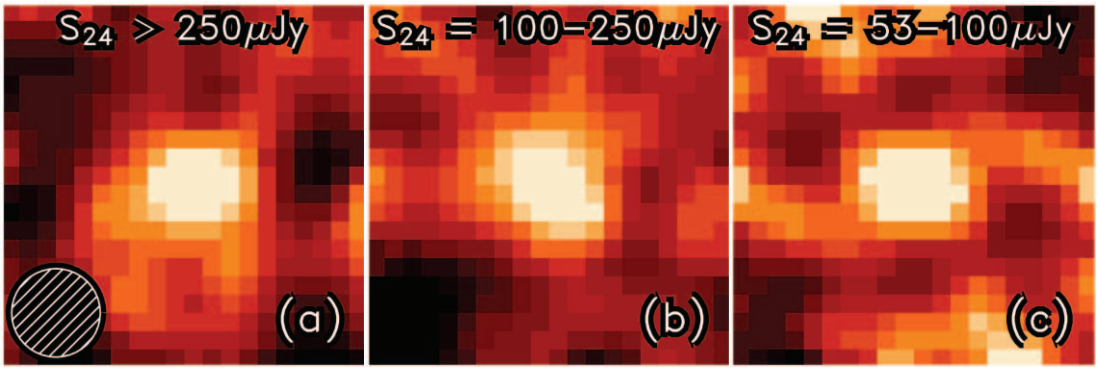

FIG. 4.—Stacked 160 μm images of ordinary IR sources at $1.5 < z_{ph} < 2.5$ (i.e., those sources without X-ray detections and IR–power-law–like colors). The panels show the 160 μm emission in bins of 24 μm flux densities of (*a*) $S_{24} > 250$ μJy, (*b*) $100 \leq S_{24}/\mu\text{Jy} < 250$, and (*c*) $53 < S_{24}/\mu\text{Jy} < 100$. Each panel shows a region approximately $170'' \times 170''$ (roughly 5 times the 160 μm PSF FWHM), at a scale of $8''$ pixel^{-1}. The filled circle, inset in panel *a*, has a diameter equal to the PSF FWHM.

density limit affect the stacked measurement. Changing the limit of the highest flux density bin from >250 to >500 μJy (or values between) has no affect on the measured S_{70}/S_{24} from the stacking, although we find that the uncertainty on the stacked value increases as the number of sources decreases in the higher flux density subamples. We do observe an increase in the stacked S_{70} measurement as we decrease limit of the highest flux density bin to values less than 250 μJy. Therefore, our choice of 250 μJy as the limit for the high flux density bin provides the logical choice to study the average S_{70} flux density as a function of S_{24}.

Figure 5 shows the average S_{70}/S_{24} ratios for the galaxies at $1.5 < z < 2.5$ split into subsamples listed in Table 2. Because the average values at 160 μm have lower S/N, we do not display them graphically. For ordinary IR sources, the average 70 μm flux densities range from 0.88 to 2.0 mJy over the range of 24 μm flux densities. These average values are consistent with those reported by Dye et al. (2007) using a smaller sample of galaxies at these redshifts. The S_{70}/S_{24} ratios are roughly comparable for the $53 < S_{24}/\mu\text{Jy} < 100$ and $100 < S_{24}/\mu\text{Jy} < 250$ samples with an average $S_{70}/S_{24} \approx 9$. However, ordinary IR sources with $S_{24} > 250$ μJy have a S_{70}/S_{24} ratio of $\approx$5, significantly lower than that measured for fainter S_{24} sources (although within the uncertainty for the faintest 24 μm subsample).

The S_{70}/S_{24} ratios for X-ray sources show little dependence on the 24 μm flux density. Although the range of S_{70}/S_{24} ratios for the X-ray sources with $53 < S_{24}/\mu\text{Jy} < 250$ is large owing to the uncertainties, these X-ray sources have lower S_{70}/S_{24} ratios than the ordinary IR sources of comparable 24 μm flux density. Interestingly, the X-ray and ordinary IR sources with $S_{24} > 250$ μJy have comparable S_{70}/S_{24} ratios, possibly implying a similar emission source for the IR emission.

The IR–power-law sources with $53 < S_{24}/\mu\text{Jy} < 250$ have S_{70}/S_{24} ratios generally larger than the X-ray sources of comparable 24 μm flux density, and are consistent with the S_{70}/S_{24} ratios of the ordinary IR galaxies. However, the IR–power-law galaxies with $S_{24} > 250$ μJy have $S_{70}/S_{24} \approx 8$, larger than the X-ray and ordinary IR subsamples.

4. DISCUSSION

In this section we discuss the ramification of the average 70 and 160 μm flux density ratios have for the interpretation of the IR emission from distant galaxies. Because we detect the average 160 μm images with low significance, we focus the discussion on the more robust S_{70}/S_{24} values. However, we use the 160 μm flux densities to constrain the IR luminosities of distant galaxies in § 4.3. We begin with a discussion of the expected S_{70}/S_{24} ratios of galaxies at $1.5 < z < 2.5$ for theoretical models and empirical templates for the IR emission of galaxies. We then use models and templates to constrain the total IR luminosity from star formation and AGN in high-redshift galaxies.

TABLE 2
AVERAGE MIPS FLUX DENSITIES FOR $1.5 < z < 2.5$ GALAXIES

S_{24} Range (μJy)	N	$\langle S_{24}\rangle$ (μJy)	$\langle S_{70}\rangle$ (mJy)	$\delta(\langle S_{70}\rangle)$ (mJy)	$\langle S_{160}\rangle$ (mJy)	$\delta(\langle S_{160}\rangle)$ (mJy)
Ordinary IR Sources						
≥250	48	380	2.0	0.5	4.6	2.6
[100, 250)	149	160	1.5	0.3	5.1	2.2
[53, 100)	77	95	0.88	0.35	4.6	2.6
X-Ray Sources						
≥250	17	480	2.2	0.7	7.1	4.3
[53, 250)	28	150	0.67	0.50	3.4	3.0
IR–Power-Law Sources						
≥250	24	530	4.0	0.7	10.5	4.3
[53, 250)	52	170	1.4	0.5	3.8	2.7

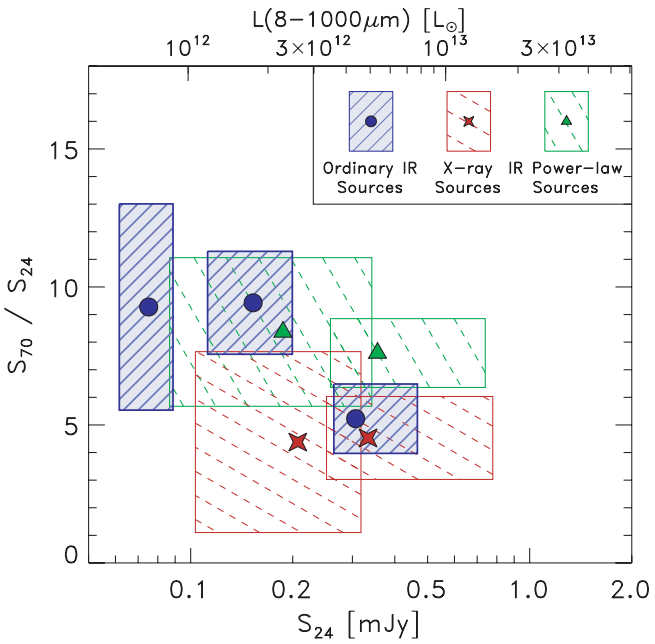

FIG. 5.—Measured S_{70}/S_{24} ratios of galaxies at $1.5 < z < 2.5$ derived from stacking 24 μm–detected sources in the 70 μm image. The symbols show the measured S_{70}/S_{24} ratios from the stacked images for the ordinary IR sources (without X-ray detections of IR–power-law–like colors; *blue circles*), X-ray sources (*red stars*), and IR–power-law sources (*green triangles*), as a function of 24 μm flux density. The horizontal width of each box shows range of the 24 μm flux density distribution within the 68 percentile for the sources in each subsample. The vertical size of a box shows the 68% confidence interval on the average flux density given the measured value and the number of sources in the stack (see text). The upper axis shows the total L_{IR}, corresponding to the measured 24 μm flux density at $z = 2$ and using bolometric corrections from Dale & Helou (2002) IR templates.

4.1. *On the Interpretation of S_{70}/S_{24} Ratios of $z = 2$ Galaxies*

There are many suites of empirical models and templates describing the IR SEDs of galaxies (e.g., Silva et al. 1998; Devriendt et al. 1999; Rowan-Robinson 2001; Chary & Elbaz 2001; Dale & Helou 2002; Lagache et al. 2003; Siebenmorgen & Krügel 2007). Here, we use primarily two sets, the empirical model templates of Dale & Helou (2002, hereafter DH02) and the theoretical models of Siebenmorgen & Krügel (2007, hereafter SK07), to study how the 24 and 70 μm flux densities of $1.5 < z < 2.5$ galaxies relates to the total IR luminosity. SK07 generated theoretical IR SEDs for stellar populations and AGNs embedded in clouds of dust and gas for a wide range of model ionization luminosity, cloud size and density, and extinction. SK07 showed that combinations of these model parameters fit the IR SEDs of known local IR-luminous galaxies.

DH02 parameterized their models by heating intensity. Following Lagache et al. 2003), we use an empirical model, which assigns each DH02 template to a given L_{IR} for its *IRAS* S_{60}/S_{100} color using the empirical equation of Marcillac et al. (2006). Lagache et al. showed that this broadly matches local *IRAS* and *IRAS* submillimeter color distributions as a function of L_{IR}, although this does not allow for dispersion in the IR colors (e.g., Chapman et al. 2003). Marcillac et al. (2006) presented evidence that these models provide reasonable agreement between total IR luminosities derived from the rest-frame 8–15 and 15–24 μm emission, and from the radio emission for galaxies with $L_{IR} \lesssim 10^{12}\ L_{\odot}$ and $z \lesssim 1$, supporting the assertion that these models represent the mid-IR properties of high-redshift galaxies.

Figure 6 shows the predicted 24 and 70 μm flux densities for the DH02 and SK07 models as observed at $z = 2$ (rest-frame 8 and 24 μm) as a function of model L_{IR}. The 24 and 70 μm flux densities for $z = 2$ galaxies predicted by the DH02 model increase monotonically with L_{IR}. The SK07 models predict a large range of flux density for a given L_{IR}, spanning approximately an order of magnitude in S_{24} and $\sim$0.5 dex in S_{70}. For the SK07 models, the median value and the range of flux densities within the 68 percentile for a given L_{IR} generally increases in a similar fashion to

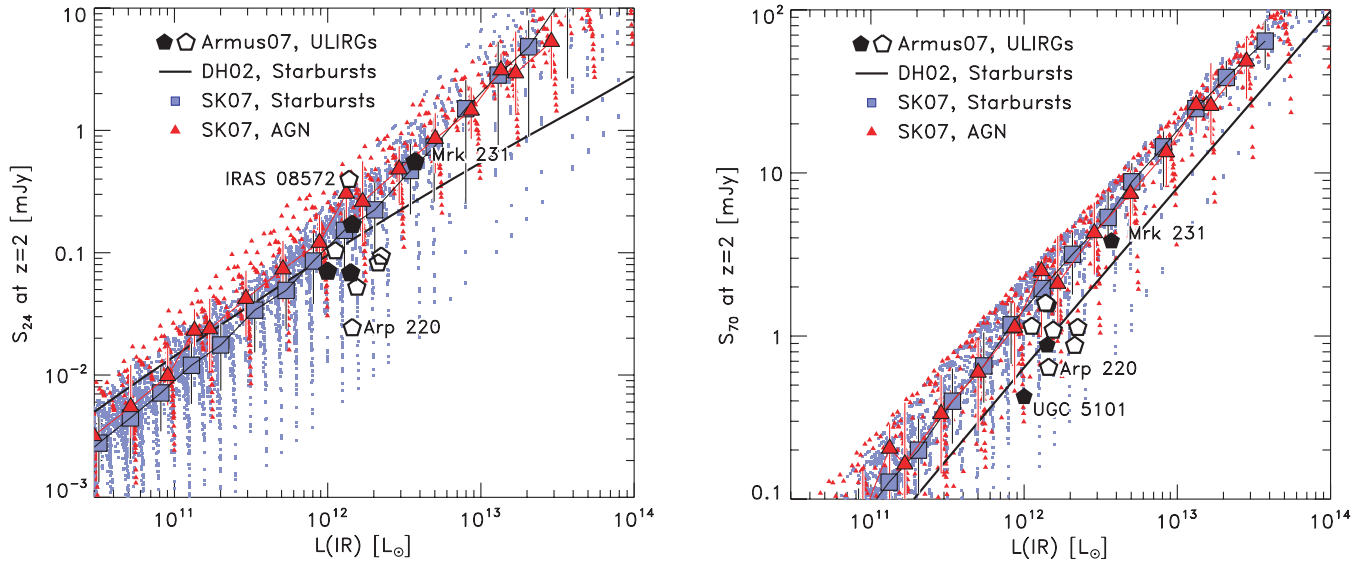

FIG. 6.—Predicted MIPS flux densities for galaxy models observed at $z = 2$. The left panel shows the 24 μm flux densities, and the right panel shows the 70 μm flux densities as a function of total IR luminosity, $L_{IR} \equiv L(8\text{–}1000\ \mu\text{m})$. In each panel the thick, solid line shows the prediction for our fiducial model of Dale & Helou (2002; DH02). Small, filled boxes and triangles show predictions for the star-forming and AGN theoretical models of Siebenmorgen & Krügel (2007; SK07), respectively. Large boxes and triangles with solid vertical lines show the median and the range within the 68 percentile for the SK07 models. The large pentagons show the expected MIPS flux densities for the *IRAS*-selected ULIRGs of Armus et al. (2007) if observed at $z = 2$. Filled pentagons show those ULIRGs with high X-ray to far-IR luminosities. ULIRGs with extreme flux densities are labeled.

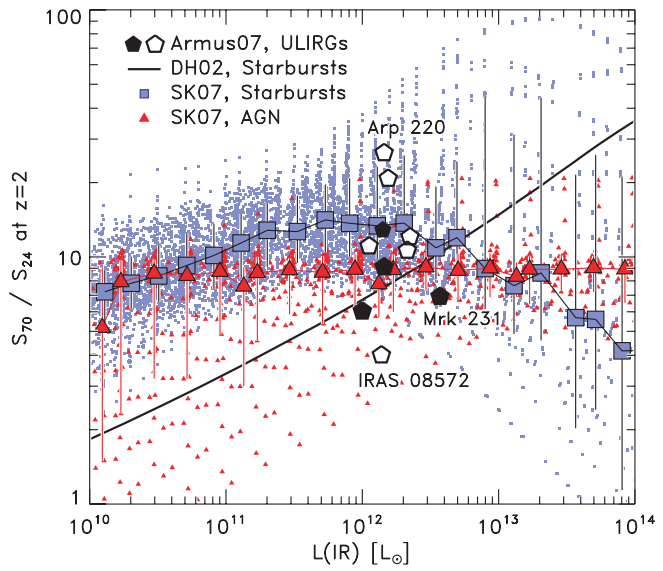

FIG. 7.—Predicted S_{70}/S_{24} ratio at $z = 2$ as a function of L_{IR} for the DH02 and SK07 models. As in Fig. 6, the thick, solid line shows the prediction for the empirical DH02 models, and the filled squares and triangles show the SK07 theoretical models for star-forming galaxies and AGNs, respectively. Large, filled symbols and vertical lines show the median andthe range within the 68 percentile for the SK07 models. The large pentagons show the expected S_{70}/S_{24} ratios for the *IRAS*-selected ULIRGs of Armus et al. (2007) if observed at $z = 2$. Filled pentagons show those ULIRGs with high X-ray to far-IR luminosities. ULIRGs with the extreme ratios are labeled.

the DH02 models (although these median values have no physical meaning because any model is as physical as the next). Interestingly, the DH02 and SK07 models predict different L_{IR} for $z = 2$ sources with bright S_{24}. A $S_{24} = 1$ mJy source at $z = 2$ would have $L_{IR} \approx 3 \times 10^{13}\ L_{\odot}$ with the DH02 model, compared to $L_{IR} \approx 6 \times 10^{12}\ L_{\odot}$ for the median SK07 model (although possible SK07 models encompass the DH02 model value for any L_{IR}).

Observations of local *IRAS*-selected ULIRGs would have observed-frame 24 and 70 μm flux densities at $z = 2$ generally consistent with the models, but with appreciable scatter. Figure 6 shows the expected 24 and 70 μm flux densities for ULIRGs from Armus et al. (2007) at $z = 2$. The expected S_{70} and L_{IR} for the ULIRGs are within a factor of order 2 of the DH02 models. However, while many of the ULIRGs of Armus et al. have S_{24} and L_{IR} within a factor of $\sim$2 of the DH02 model, there are outliers that span a large range in S_{24}, from $\approx$25 μJy for Arp 220 to $\approx$400 μJy for IRAS 08572+3915.

Figure 7 shows the S_{70}/S_{24} ratio for the DH02 and SK07 models observed at $z = 2$ as a function of L_{IR}. The S_{70}/S_{24} ratios of the DH02 models increase monotonically with L_{IR}, indicating that more luminous sources have higher S_{70}/S_{24} ratios (although this is in contrast to the observations, see § 4.2 below). The SK07 models span a large range of S_{70}/S_{24} ratio at fixed L_{IR} owing to the large range of parameter possibilities. Interesting however, all of the SK07 models for star-forming galaxies with $L_{IR} < 10^{12}\ L_{\odot}$ have S_{70}/S_{24} ratios significantly larger than the DH02 model. We suspect this is because although the SK07 models include many individual OB-star associations, they limit the models to spherical geometry. Also, the SK07 models may not include the superposition of intense star-forming regions with additional IR emission from extended cold dust in a galactic disk. The DH02 models are based on empirical observations of local star forming galaxies, designed to match *IRAS* color-luminosity relations, and include the complex emission from galaxies.

SK07 models for star-forming galaxies with $L_{IR} \sim 10^{12}$–$10^{14}\ L_{\odot}$ span 2 orders of magnitude in S_{70}/S_{24} ratio. The median S_{70}/S_{24} ratio for these models declines with increasing L_{IR}, in contrast to our DH02 model. Thus, the SK07 star-forming–galaxy model predicts that the most luminous galaxies may have low S_{70}/S_{24} ratios (broadly consistent with the observations; see below). In contrast, SK07 models for AGN span the largest range of S_{70}/S_{24} ratio for less luminous objects. The SK07 AGN models with $L_{IR} > 10^{12}\ L_{\odot}$ span a range of S_{70}/S_{24} ratios, from $\approx$5 to 20.

The ULIRGs from Armus et al. (2007) have flux densities at $z = 2$ that span almost an order of magnitude in S_{70}/S_{24} ratio. Most of this scatter results from the range of S_{24}. Excluding Arp 220 and IRAS 2491−1808 with S_{70}/S_{24} ratios >20, and IRAS 08572+3915 with a S_{70}/S_{24} ratio $\approx$4, the other ULIRGs have S_{70}/S_{24} ratios comparable to the DH02 models and the SK07 median range. The ULIRGs with low hard X-ray to IR luminosity ratios are presumably dominated by star formation. These objects span the full range of S_{70}/S_{24} ratios, suggesting that star-forming ULIRGs have diverse mid-IR flux ratios, even at comparable total IR luminosity. Focusing instead on the ULIRGs with high hard X-ray to IR luminosity ratios that presumably have some contribution from AGNs, these objects match the S_{70}/S_{24} flux ratios of the SK07 AGN models, as well as the DH02 predictions. The expected S_{70}/S_{24} ratios from the local ULIRGs do not depend on the ratio of the X-ray to IR luminosity. Observations of objects with a range of hard X-ray to IR luminosity ratios at other L_{IR} could perhaps better discriminate AGNs and star-forming ULIRG samples.

4.2. *Constraints on the Far-IR Spectral Energy Distributions of High-Redshift Galaxies*

Figure 8 compares the average S_{70}/S_{24} ratios for the $1.5 < z_{ph} < 2.5$ galaxies from the stacking analysis to expected ratios for local empirical template SEDs. The cyan swath in Figure 8 shows the expected S_{70}/S_{24} ratios as a function of 24 μm flux density for the IR model templates of DH02 with $1.5 < z < 2.5$. For comparison, the magenta swath shows the expected S_{70}/S_{24} as a function of 24 μm flux density from Chary & Elbaz (2001, hereafter CE01) for the same redshift range. The figure also shows the expected S_{70}/S_{24} ratios and 24 μm flux densities at $z = 2$ for the local ULIRGs (Armus et al. 2007), which show a wide range in diversity in their mid-IR properties, as discussed above. Here, we discuss the S_{70}/S_{24} ratios for the galaxy samples at $1.5 < z_{ph} < 2.5$.

4.2.1. *Ordinary IR Sources*

The IR luminosities of ordinary IR galaxies at $1.5 < z < 2.5$ (i.e., objects without X-ray detections or IR–power-law–like colors) with $53 < S_{24}/\mu\text{Jy} < 100$ are 10^{11}–$10^{12}\ L_{\odot}$, using the 24 μm emission with bolometric corrections from either the DH02 or CE01. The stacked 70 μm flux density for sources at $1.5 < z < 2.5$ with $53 < S_{24}/\mu\text{Jy} < 100$ has S/N < 3, and some caution must be applied. Nevertheless, the measured average S_{70}/S_{24} ratio for these sources match the values expected from the DH02 and CE01 models. They are consistent with the theoretical SK07 models, which predict that star-forming galaxies with $53 < S_{24}/\mu\text{Jy} < 100$ and $L_{IR} \sim 10^{11}$–$10^{12}\ L_{\odot}$ have $S_{70}/S_{24} \sim 8$–15. Four of the Armus et al. (2007) ULIRGs would have $53 < S_{24}/\mu\text{Jy} < 100$ observed at $z = 2$. These sources have $L_{IR} = 1$–$2 \times 10^{12}\ L_{\odot}$, and S_{70}/S_{24} ratios 6–13, consistent with the measured values from the stacking.

Sources with $1.5 < z < 2.5$ and $100 < S_{24}/\mu\text{Jy} < 250$ have $L_{IR} = 1$–$3 \times 10^{12}\ L_{\odot}$ using bolometric corrections from DH02 (and somewhat larger L_{IR} using CE01). The measured S_{70}/S_{24} ratio from the stacking analysis has S/N = 5. Inspection of Figure 8

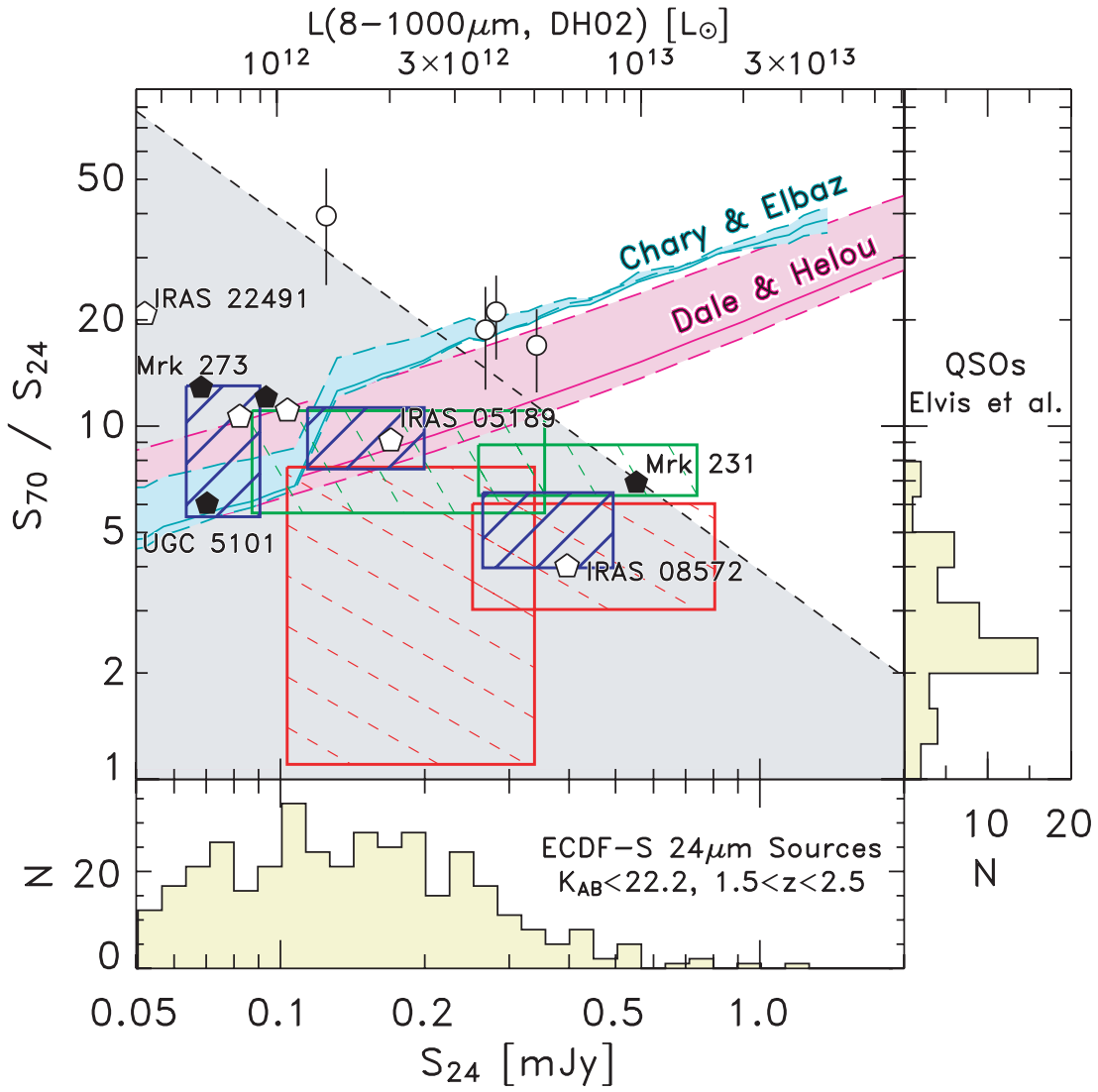

FIG. 8.—Comparison of the S_{70}/S_{24} ratios of $1.5 < z < 2.5$ galaxies from the stacking analyses to model expectations. Hatched boxes correspond to the average values with hatch pattern and colors as in Fig. 5. Circles show those galaxies with $1.5 < z < 2.5$ detected at 70 μm. The pentagons show the expected S_{70}/S_{24} ratios for the *IRAS*-selected ULIRGs of Armus et al. (2007) if observed at $z = 2$. Filled pentagons show those ULIRGs with high X-ray to far-IR luminosities. ULIRGs with the extreme ratios are labeled. The magenta-shaded swath shows the expected flux ratios for the Dale & Helou (2002) models for $1.5 < z < 2.5$. The cyan-shaded swath shows the expected flux ratios for Chary & Elbaz (2001) models over the same redshift range. In both cases the solid line shows the expected value at $z = 2$. The shaded region shows the area below the MIPS 70 μm 50% completeness limit (3.9 mJy). The top abscissa shows the total L_{IR} corresponding to S_{24} at $z = 2$ using bolometric corrections from the Dale & Helou models. The right panel shows the distribution of S_{70}/S_{24} ratios for QSO SEDs taken from Elvis et al. (1994). A source with constant power in νf_ν has $S_{70}/S_{24} = 2.9$. The bottom panel shows the S_{24} distribution of the K_s-band sample with $1.5 < z < 2.5$.

shows that the observed S_{70}/S_{24} ratio is consistent with the DH02 model, but lower by a factor of $\sim$2 than expected from the CE01 model. The measured S_{70}/S_{24} ratio is on the low end of the values predicted by the theoretical SK07 models. The SK07 models that reproduce the measured S_{70}/S_{24} ratio for these galaxies have high extinction, $A_V = 2.2$–6.7 mag (corresponding to $A_{UV} = 6$–19 mag at 1500 Å), whereas the range of all SK07 models within the 68 percentile at these IR luminosities have even larger extinctions, $A_V = 7$–37 mag (and in comparison, the SK07 model to Arp 220 has $A_V = 72$ mag).

If these models accurately describe the high-redshift galaxies, then they have high extinction. However, we note that the *minimum* extinction in the SK07 models is $A_V = 2.2$, suggesting that possible models with lower extinction may fit the measured flux density ratios equally well. For example, Daddi et al. (2007a) find that most $z \sim 2$ *BzK*-selected galaxies have relatively low ("optically thin") dust attenuations, corresponding to $A_{UV} \sim$ 2–6 mag. However, most of the $z \sim 2$ galaxies in their sample have low 24 μm flux densities, $S_{24} \ll 100$ μJy. Furthermore, the *BzK* selection may miss objects with high dust obscuration, such as submillimeter galaxies or distant red galaxies (e.g., see Reddy et al. 2006). As with other observations of local and distant galaxies, a galaxy's extinction increases with bolometric luminosity (e.g., Wang & Heckman 1996; Reddy et al. 2006). Our comparison against the SK07 models implies that the sources with $100 < S_{24}/\mu\text{Jy} < 250$ at $z = 2$ have relatively high extinction as well, consistent with these other results.

Two of the local ULIRGs from Armus et al. (2007) would have $100 < S_{24}/\mu\text{Jy} < 250$ at $z = 2$, IRAS 05189-2524 and IRAS 15250+3609. They have $L_{IR} \approx 10^{12}$ $L_\odot$, and S_{70}/S_{24} ratios of ≈ 9 and 11, comparable to the measured values from the stacking. Both of these ULIRGs have emission and absorption

features in their mid-IR spectra that are fairly average in the sample of Armus et al. (2007). To measure the strength of the mid-IR emission features directly for $1.5 < z < 2.5$ galaxies with $100 < S_{24}/\mu\mathrm{Jy} < 250$ requires prolonged exposures with mid-IR spectrographs—the Infrared Spectrograph (IRS) on board *Spitzer* requires $\sim$10 hr to obtain spectra of objects with $S_{24} \sim 150$–250 μJy (Teplitz et al. 2007)—or by targeting gravitationally lensed 24 μm sources with IRS (e.g., Rigby et al. 2007). Nevertheless, the few published IRS spectra of galaxies at these redshifts and 24 μm flux density show that the mid-IR emission features are consistent with local IR-luminous galaxies. Therefore there is little evidence that the $1.5 < z < 2.5$ galaxies with $100 < S_{24}/\mu\mathrm{Jy} < 250$ have abnormally strong or weak mid-IR features.

Ordinary IR galaxies with $S_{24} > 250$ μJy and $1.5 < z < 2.5$ have lower S_{70}/S_{24} ratios compared to the fainter 24 μm sources. Interestingly, both the DH02 and CE01 models have S_{70}/S_{24} ratios larger than the measured ratio by factors of $\approx$2–3. This is striking because if there existed a substantial population of sources with $S_{24} > 250$ μJy and S_{70}/S_{24} ratios high as the DH02 or CE01 model predictions, then these sources would have $S_{70} \gtrsim$ 3–10 mJy and would have been detected directly in the 70 μm data. Of the 89 sources with $S_{24} > 250$ μJy (including 17 with X-ray detections and 24 with IR–power-law SEDs), we detect only three at 70 μm (all with $3 < \mathrm{S/N} < 4$). Interestingly, these 70 μm–detected objects have S_{70}/S_{24} ratios consistent with the DH02 and CE01 models. Such sources must be extremely rare—they represent only $3\% \pm 2\%$ (3/89) of $S_{24} > 250$ μJy sources. Even more extreme (and rare) $S_{24} > 750$ μJy and $S_{24} > 900$ μJy sources at $z \sim 2$ studied by Houck et al. (2005) and Yan et al. (2007) respectively, have S_{70}/S_{24} flux density ratios < 10 (E. Le Floc'h 2006, private communication; K. Tyler et al. 2007, in preparation; Sajina et al. 2007), even though they were selected over much larger fields than used here ($\simeq$9 and $\simeq$4 deg^2, respectively), consistent with our findings.

Therefore, the brightest 24 μm sources at $1.5 < z < 2.5$ have low S_{70}/S_{24} ratios. These galaxies may suffer from unusually strong mid-IR emission features from PAHs, which would boost the observed 24 μm flux density and lower S_{70}/S_{24}. Several published mid-IR spectra data sets from *Spitzer* now exist for galaxies with $S_{24} > 250$ μJy and $z \sim 2$ (Houck et al. 2005; Yan et al. 2005; Weedman et al. 2006a, 2006b). While some do show strong PAH emission, most have rather featureless spectra. Therefore, the low S_{70}/S_{24} flux density ratios are likely not solely a result of unusually strong mid–IR emission features.

The S_{70}/S_{24} flux density ratios of the $S_{24} > 250$ μJy sources with $1.5 < z_{\mathrm{ph}} < 2.5$ are comparable to SK07 theoretical star-forming models with moderate extinction, $A_V = 2.2$ mag, and small physical sizes, $R = 0.35$ kpc. These sizes are smaller than the rest-frame optical radii of $z \sim 2$ galaxies (Trujillo et al. 2004; Papovich et al. 2005), which is consistent as the IR-emitting region is likely not larger than the optical size. A compact IR-emitting region implies these objects have warmer dust temperatures ($T \sim 40$–60 K) compared to high-redshift submillimeter-selected galaxies, which require colder dust temperatures ($T \sim 20$ K, e.g., Chapman et al. 2005) and an extended emission region to reproduce the submillimeter number counts ($R \gtrsim 5$ kpc; Kaviani et al. 2003). Indeed, Egami et al. (2004) and Pope et al. (2006) find that the average IR SEDs for submillimeter sources are consistent with the IR emission from cooler dust ($\sim$30 K). These lower dust temperatures are similar to that of Arp 220, which would have $S_{70}/S_{24} \approx 30$ if observed at $z = 2$, strongly in contrast to the $S_{24} > 250$ μJy sample ($S_{70}/S_{24} \approx 6$). Therefore, the nature of the IR emission in bright 24 μm–sources at $1.5 < z < 2.5$ is likely different from that of submillimeter-selected samples. If star formation powers the IR emission in bright 24 μm sources at $1.5 < z < 2.5$, then these sources are likely compact, presumably with higher dust temperatures (e.g., Chanial et al. 2007).

Alternatively, the $S_{24} > 250$ μJy sources at $1.5 < z_{\mathrm{ph}} < 2.5$ may be powered by AGNs or starburst/AGN composites. Indeed, Daddi et al. (2007b) present evidence that sources at $z \sim 2$ with anomalously high 24 μm flux densities compared to other star formation indications host heavily obscured AGN. As noted previously, the S_{70}/S_{24} ratios are comparable to those of the X-ray with $S_{24} > 250$ μJy. Given that even deep X-ray data miss a high fraction of AGN (e.g., Donley et al. 2007), we expect that some portion of the $S_{24} > 250$ μJy population has an AGN contribution. In this case, similar physical emission mechanisms may be at work in all the $S_{24} > 250$ μJy samples.

4.2.2. *X-Ray Sources*

The measured S_{70}/S_{24} ratios for X-ray sources at $1.5 < z < 2.5$ span the empirical range observed for QSOs (Elvis et al. 1994). X-ray sources with $S_{24} > 250$ μJy have S_{70}/S_{24} ratios on the red tail of the QSO distribution. This is probably a result that our sample contains 24 μm–bright X-ray sources, which presumably have IR colors similar to redder, optically selected QSOs. The stacked S_{70}/S_{24} ratio for X-ray sources with $53 < S_{24} < 250$ μJy has low S/N. It may be that the IR emission in these sources stems both from AGNs and star formation processes (as in the case of Mrk 231; e.g., Armus et al. 2007). In this case, an AGN dominates the mid-IR SED in the X-ray sources, heating dust to warmer temperatures, which boosts the observed-frame 24 μm emission and lowers the S_{70}/S_{24} ratios compared to what is typically observed in starbursts. Both Alexander et al. (2005) and Frayer et al. (2003) show evidence that submillimeter-selected galaxies at $z \gtrsim 2$ show evidence for simultaneous AGN and star formation activity, where dust heated by the starburst dominates the submillimeter emission. To test for evidence of colder dust in the X-ray–detected galaxies requires flux density measurements at longer wavelengths, i.e., at rest-frame $\lambda > 100$ μm (see, e.g., Le Floc'h et al. 2007).

4.2.3. *IR–Power-Law Sources*

The IR–power-law sources with $1.5 < z < 2.5$ have similar S_{70}/S_{24} ratios for the $100 < S_{24}/\mu\mathrm{Jy} < 250$ and $S_{24} > 250$ μJy sample, although the S_{70}/S_{24} ratio for IR–power-law sources with $53 < S_{24}/\mu\mathrm{Jy} < 250$ has $\mathrm{S/N} \approx 3$. Nevertheless, IR–power-law source have low S_{70}/S_{24} ratios compared to either the star-forming empirical or theoretical SED models given their 24 μm flux densities. SK07 AGN models that match the S_{70}/S_{24} ratios of IR–power-law sources with $53 < S_{24}/\mu\mathrm{Jy} < 250$ span a wide range of model parameter space, providing few useful constraints. The SK07 models for AGN with $S_{24} > 250$ μJy that match the IR power-law source S_{70}/S_{24} ratios span a wide range of extinction, $A_V = 1$–128 mag. Most of the models require obscuring regions with sizes 8–16 kpc. Therefore, if solely an AGN is responsible for the IR emission, the extinction region may extend to the entire host galaxy. Alternatively, a more plausible scenario is that the IR emission in these galaxies results from a composite starburst/AGN.

4.3. *Implications for the Total IR Luminosities of High-Redshift Galaxies*

The average 24, 70, 160 μm flux densities constrain the shape and normalization of the average far-IR SED—and thus the total IR luminosity—of the typical 24 μm source at $1.5 < z < 2.5$. Because we have only the average flux densities, these results apply only on *average* for the 24 μm source population at $1.5 < z < 2.5$.

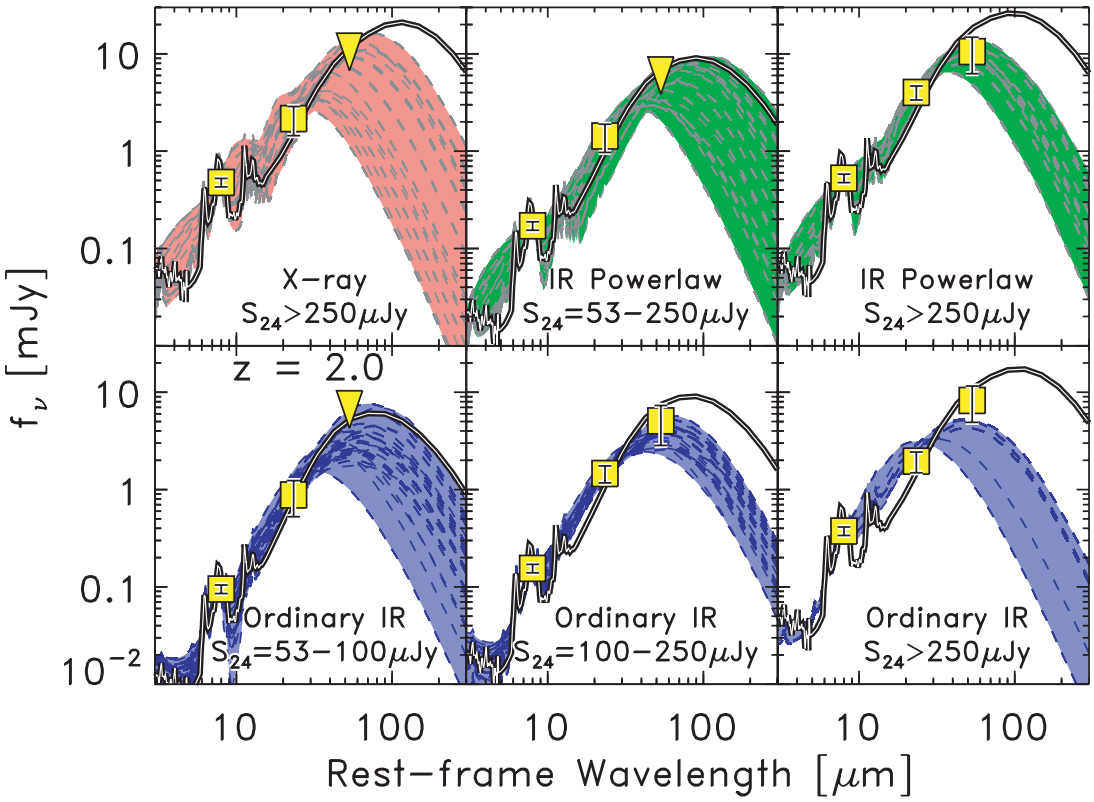

FIG. 9.—Model fits for $z = 2$ to the 24, 70, and 160 μm flux densities data listed in Table 2. The yellow squares in each panel show the measured flux densities. Downward triangles show the 1 σ upper limit for measured flux densities in Table 2 with S/N < 2. In each panel, the thick line shows the best-fit DH02 model to the data, where the normalization is a free parameter. The shaded area shows the range of SK07 models that fit the data (without allowing for a normalization of the model luminosities). The IR–power-law sources show the results for $53 < S_{24}/\mu\text{Jy} < 250$ μJy and $S_{24} > 250$ μJy. The X-ray sources show the results for $S_{24} > 250$ μJy only because X-ray sources with lower 24 μm flux density have S/N < 2 for both the 70 μm and 160 μm stacked measurements. For both the X-ray and IR power-law sources we use the SK07 AGN models for the fit. We fit the SK07 models to the data for the ordinary IR sources.

There is likely significant variation from object to object. Indeed, if the *IRAS*-selected ULIRGs of Armus et al. (2007) were observed at $z = 2$, then they would show a large variation between $L_{\rm IR}$, S_{24}, and S_{70} (see Fig. 8).

We fit the measured average 24, 70, and 160 μm flux densities data in Table 2 for the ordinary IR sources, X-ray sources, and IR–power-law sources with the DH02 and SK07 model templates for model redshifts $z = 1.5$, 2.0, and 2.5. Including the analysis over the full range of redshifts, as opposed to restricting it to only the average redshift of the sample, shows how the interpretation depends as a function of redshift. For example, because the strong spectral features move through the 24 μm band at these redshifts, the redshift of the galaxy makes a sizeable difference in the interpretation of its S_{70}/S_{24} measurement. However, the fits at the three different redshifts are not statistically independent. Here, we fit the full range of DH02 template SEDs, with the model normalization as a free parameter. This allows the high-redshift galaxies to have any ionization for a given $L_{\rm IR}$. For each set of average 24, 70, and 160 μm flux densities listed Table 2, we take the IR-luminosity of the best-fitting DH02 model, scaled to match the measured flux densities. Because the SK07 models are derived for a specified set of physical input parameters, allowing variations in the normalization would change the physical conditions of the model. Therefore, we do not allow the normalization to vary. Instead, we take the IR luminosity of the best-fitting SK07 model as the IR luminosity for the set of average 24, 70, and 160 μm flux densities.

Figure 9 illustrates the best fitting models to the ordinary IR sources, X-ray sources, and IR–power-law sources assuming the fiducial redshift $z = 2$. In each panel, the thick, solid line shows the best-fit DH02 model. We show the range of SK07 models fit to the data as the shaded region, where we have repeated the model fitting to the data after randomly adjusting the measured flux densities by their 1 σ uncertainties. Although the average 160 μm flux densities have low S/N, they improve the constraints on the derived IR luminosity, especially by limiting the range of the SK07 model parameter space. Nevertheless, in many cases a fairly wide range of models fit the data, giving a spread in the inferred $L_{\rm IR}$. While the average 24, 70, and 160 μm data improve the constraints on the total IR luminosity, significant uncertainties persist. Observations at rest-frame wavelengths >100 μm are required to measure the full shape of the IR SED.

Because nearly all studies of high-redshift MIPS-detected galaxies rely on 24 μm observations only, we also compute the total IR luminosity using the 24 μm flux density and our fiducial DH02 model (see above; e.g., Le Floc'h et al. 2005, Papovich et al. 2006). While the DH02 models are inappropriate for AGNs, most work in the literature uses similar SEDs to convert the 24 μm flux density to IR luminosity. Therefore, it is prudent for us to compare against them here. We do not infer the $L_{\rm IR}$ from the 24 μm flux density using the SK07 models as these models span such a large range of $L_{\rm IR}$ for a given S_{24} at these redshifts (see Fig. 6).

Figure 10 compares the total IR luminosities derived from the best-fit models to the 24, 70, and 160 μm flux densities [$\equiv L_{\rm IR}(24, 70, 160\mu\text{m})$] to the IR luminosity estimated solely from the 24 μm flux density [$\equiv L_{\rm IR}(24\ \mu\text{m})$]. For all redshifts $1.5 < z < 2.5$, the $L_{\rm IR}$(24, 70, 160 μm) for ordinary IR sources

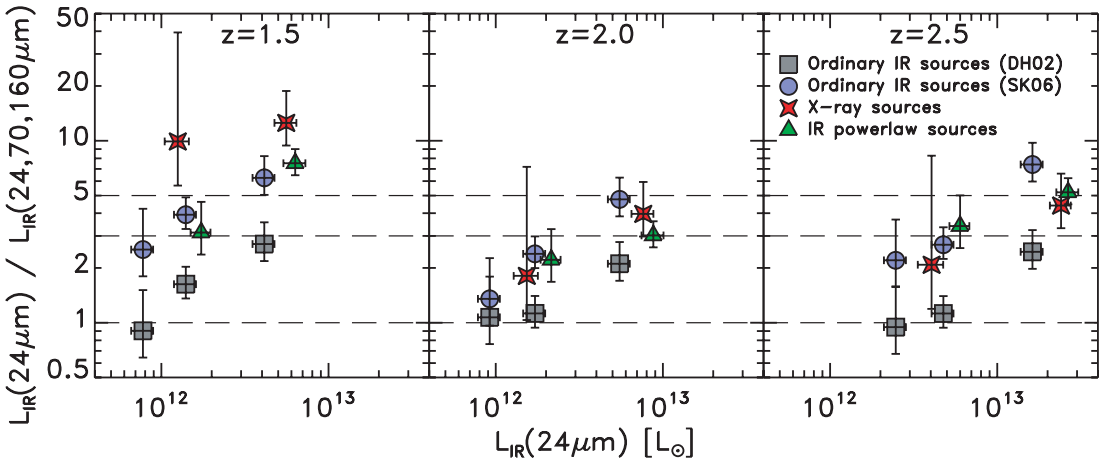

FIG. 10.—Comparisons of L_{IR}(24 μm) to L(24, 70, 160 μm). The L_{IR}(24 μm) are derived solely using the 24 μm flux density, S_{24}, and specified redshift with the DH02 bolometric corrections. The L_{IR}(24, 70, 160 μm) are derived using both the SK07 or DH02 models for bolometric corrections. The symbols show the results for ordinary IR sources (without X-ray detections or IR–power-law–like colors; blue circles for SK07 models; gray squares for DH02 models, see plot inset), X-ray sources (*red stars*), and IR–power-law sources (*green triangles*) using the flux densities listed in Table 2. The results for the ordinary IR sources are shown using both the DH02 and star-forming SK07 models. The L_{IR}(24, 70, 160 μm) values for the X-ray sources and IR–power-law sources are derived using the SK07 AGN models. Each panel shows the fit using models at $z = 1.5$, 2, and 2.5, as labeled. The horizontal dashed lines show luminosity ratios of 1, 3, and 5.

and $100 < S_{24}/\mu\text{Jy} < 250$ or $53 < S_{24}/\mu\text{Jy} < 100$ are within a factor of <3 of L_{IR}(24 μm). This is true in the comparison between L_{IR}(24 μm) and L_{IR}(24, 70, 160 μm) for either the DH02 or SK07 models.

The ordinary IR sources with $S_{24} > 250$ μJy generally have larger L_{IR}(24 μm)/L_{IR}(24, 70, 160 μm) than fainter 24 μm sources. The L_{IR}(24, 70, 160 μm) derived from the DH02 models are within a factor of $\lesssim$3 of L_{IR}(24 μm). In contrast L_{IR}(24, 70, 160 μm) derived with the SK07 models are $\approx$4–8 times lower than L_{IR}(24 μm).

The L_{IR}(24, 70, 160 μm) derived with the DH02 models is always a factor of $\approx$2 lower than L_{IR}(24, 70, 160 μm) derived from the SK07 models. This results from the intrinsic difference between the shape of the SED in the theoretical and empirical models. As discussed above, this difference results because in the theoretical models the IR emission comes from embedded OB-star associations. Compared to the empirical model, which includes the integrated emission from complex galactic structures, the theoretical models require warmer dust temperatures to match the observed flux densities, with increased relative emission at rest-frame $\lambda \sim 10$–30 μm and decreased relative emission at rest-frame $\lambda > 50$ μm (see Fig. 9). The current data do not favor either the IR SED shape from the theoretical or empirical model, and constraints at rest-frame wavelengths longer than 50 μm are needed. The different models give a range of uncertainty arising from the shape of the choice of SED, which accounts for the factor of 2.

While we have not included the analysis of the CE01 models in Figure 10, we make some qualitative comparisons here. Given that the CE01 and DH02 models give similar expected S_{70}/S_{24} ratios for sources with $S_{24} \lesssim 100$ μJy at $z = 2$ (Fig. 8), we expect similar results between these models for the faint sources. At higher 24 μm flux densities, the CE01 models predict higher S_{70}/S_{24} ratios, and thus we expect the difference between L_{IR}(24 μm) and L_{IR}(24, 70, 160 μm) to be larger for CE01 than for DH02.

The ratio of L_{IR}(24 μm) to L_{IR}(24, 70, 160 μm) for the X-ray and IR–power-law samples depends strongly on the assumed model redshift and S_{24}. For X-ray and power-law sources with $S_{24} > 250$ μJy, this ratio ranges from a factor of $\gtrsim$10 at $z = 1.5$ to $\sim$3 at $z = 2.5$. The reason for the dramatic decrease in IR luminosity ratio with increasing redshift is because at $z = 1.5$ the SK07 AGN models that fit the data have steeply rising mid-IR SEDs with very hot dust temperatures, peaking at $\sim$30 μm. The DH02 models place the 24 μm band in the gap between strong PAH features at 7.7 and 11 μm, with the peak emission at $\sim$100 μm, producing higher IR luminosity for the same mid-IR flux density.

4.4. *Implications for the Star Formation of High-Redshift Galaxies*

In this section we study the implications the stacking results have for the total IR luminosities and the SFRs for individual 24 μm–detected galaxies at high redshifts. To illustrate this, we compute the total IR luminosities for all the $1.5 < z_{ph} < 2.5$ galaxies with $S_{24} > 53$ μJy using two methods. We used the S_{24} and the photometric redshift of each galaxy to infer its total IR luminosity, L_{IR}(24 μm), using bolometric corrections from our fiducial DH02 model, following the method in Le Floc'h et al. (2005) and Papovich et al. (2006). Second, we assign to each galaxy the 70 and 160 μm flux density derived from the stacking analysis, $\langle S_{70} \rangle$ and $\langle S_{160} \rangle$ for its measured S_{24}. We then fit models to the S_{24}, $\langle S_{70} \rangle$, and $\langle S_{160} \rangle$ for each galaxy at the redshift of each galaxy to derive L_{IR}(24, 70, 160 μm), following the procedure in § 4.3. For the ordinary IR sources with $S_{24} > 53$ μJy we used L_{IR}(24, 70, 160 μm) derived with the DH02 empirical models. For X-ray and IR–power-law sources with $S_{24} > 53$ μJy we used the SK07 theoretical AGN models.

Our choice to apply the DH02 models for ordinary IR sources is motivated by the fact that the theoretical SK07 models do not include additional dust components from the galaxies' ISM. Using the SK07 theoretical models would reduce the derived L_{IR} by a factor of $\approx$2 (see Fig. 10). Although we use the SK07 AGN models for X-ray sources, this may not be fair as these theoretical models allow for no IR emission due to dust heated by star formation. X-ray sources may have additional cold dust components possibly associated with star formation (e.g., Frayer et al. 2003; Alexander et al. 2005). If such additional components

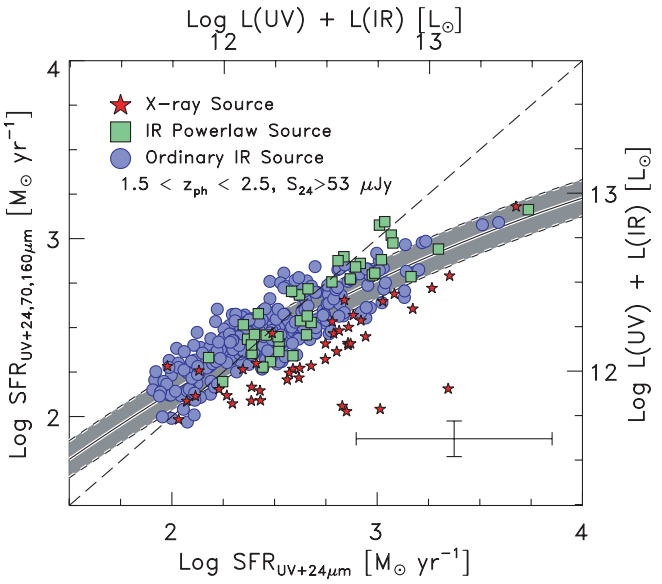

FIG. 11.—SFR derived for galaxies in the MUSYC $1.5 < z_{ph} < 2.5$ sample using only the UV and 24 μm data, $SFR_{UV+24\,\mu m}$, compared to the SFR derived using the UV and 24 μm data and the average 70 and 160 μm flux densities from the stacking analyses, $SFR_{UV+24,70,160\,\mu m}$. The right and top axes show the corresponding bolometric luminosity, $L_{bol} \equiv L_{UV} + L_{IR}$, under the assumption that star formation heats the dust producing the IR emission. Blue circles show ordinary IR sources (without X-ray detections or IR–power-law–like colors). Green squares denote IR–power-law sources (excluding X-ray sources). Red pentagrams show X-ray sources. The dashed line shows the unity relation. The shaded region shows a polynomial fit to the data, excluding the X-ray sources and IR–power-law sources (see text). The error bar shows typical errors on the derived SFRs, ≈0.5 dex for the abscissa and 0.1 dex for the ordinate.

exist in AGNs, then the L_{IR} values derived from the SK07 models may underestimate the total IR luminosity.[10]

Under the assumption that star formation is primarily responsible for the dust heating powering the IR emission, we estimate the instantaneous SFR using the bolometric luminosity, defined as the sum of the rest-frame UV and total IR luminosities of each galaxy, $\Psi/1\ M_\odot = 1.8 \times 10^{-10} \times L_{bol}/L_\odot$, where $L_{bol} \equiv (2.2 \times L_{UV} + L_{IR})$, L_{IR} is the total IR luminosity and L_{UV} is the rest-frame UV luminosity derived from the monochromatic luminosity at 2800 Å, $L_{UV} = 1.5 \times L(2800\ Å)$, uncorrected for extinction (e.g., Bell et al. 2005). The SFR to bolometric luminosity calibration assumes a Salpeter-like IMF with upper and lower mass cutoffs of 0.1 and 100 $M_\odot$ (see, e.g., Kennicutt 1998; Bell 2003; Bell et al. 2005). Figure 11 compares the SFRs derived using the 24 μm data only to the SFRs derived from the 24 μm flux density with the average 70 and 160 μm flux densities. Symbol types denote objects with X-ray detections and IR–power-law sources.

The relation in Figure 11 provides a tool for deriving SFRs for $1.5 < z < 2.5$ galaxies "corrected" using the average 70 and 160 μm flux densities given a bolometric luminosity derived from the UV and 24 μm flux. Note, however, for the 24 μm–selected sources L_{IR} constitutes the majority of the bolometric luminosity, and $L_{IR}(24,\ 70,\ 160\ \mu m)/L_{bol} = 0.85$–$1.0$ for all sources here. We fit a second-order polynomial to the data in Figure 11 (excluding X-ray and IR–power-law sources) to derive an empirical relation between the derived SFRs. The fit is valid over the range $\Psi \gtrsim 100\ M_\odot\ yr^{-1}$ $[\log(L_{bol}/L_\odot) \geq 11.8]$. The empirical relation is

$$y = \sum_{i=0}^{2} C_i x^i, \quad (1)$$

where $y \equiv \log(\Psi_{UV+24,\,70,\,160\,\mu m})$, $x \equiv \log(\Psi_{UV+24\mu m})$, where Ψ has units of $M_\odot\ yr^{-1}$, and $C = (0.37,\ 1.05,\ -0.085)$ are the polynomial coefficients. The standard error on $\log(SFR_{UV+24,\,70,\,160\,\mu m})$ is 0.1 dex, derived from the polynomial fit. The fit is indicated by the shaded band in the figure. A similar relation exists for the bolometric luminosities, L_{bol}, replacing Ψ in equation (1) with, $x \equiv \log\{[2.2 \times L_{UV} + L_{IR}(24\ \mu m)]/5.6 \times 10^9\ L_\odot\}$ and $y \equiv \log\{[2.2 \times L_{UV} + L_{IR}(24,\ 70,\ 160\ \mu m)]/5.6 \times 10^9\ L_\odot\}$.

Unsurprisingly, Figure 11 illustrates that objects with large bolometric luminosities—and thus large SFRs—inferred from their 24 μm flux densities are reduced substantially when we include the average 70 and 160 μm flux densities from the stacking analysis. As a result, some published studies using the inferred SFRs and L_{IR} for bright 24 μm–selected objects at $z \sim 2$ deserve reexamination. Several studies using data covering relatively small areas (∼100–160 arcmin^2) found that sources at $z \sim 2$ have average 24 μm flux densities, ≃100–200 μJy (Daddi et al. 2005; Caputi et al. 2006; Papovich et al. 2006; Reddy et al. 2006; Webb et al. 2006). At these flux densities our analysis shows that $L_{IR}(24\ \mu m)$ and $L_{IR}(24, 70, 160\ \mu m)$ are comparable (within a factor of 2 for the DH02 models), and the average 70 and 160 μm emission will have little influence on the conclusions of these studies. In contrast, studies of 24 μm sources at $z \sim 2$ over relatively larger areas identify many more bright 24 μm sources, where the average 70 and 160 μm sources have the most affect. For example, Pérez-González et al. (2005) find that the characteristic luminosity of the total IR luminosity function at $z = 2$ is $\approx 4 \times 10^{12}\ L_\odot$ (applying their scaling to the monochromatic rest-frame 12 μm luminosity), corresponding to $S_{24} \approx 300$ μJy. Our findings imply that IR luminosities of sources as bright or brighter than the "knee" in this luminosity function will be overestimated by factors of >2 (or greater than a factor of 4 using the SK07 models). Moreover, Houck et al. (2005) and Yan et al. (2007) study the *Spitzer* IRS spectra of $z \sim 2$ sources with $S_{24} > 0.75$ and >0.9 mJy, respectively. The total IR luminosities of these sources will be overestimated by factors of >3 (and possibly as large as an order of magnitude) using solely on the 24 μm flux densities and local templates for star-forming galaxies. Therefore, based on our stacking analysis at 70 and 160 μm, the bolometric luminosities and SFRs of bright 24 μm galaxies at $1.5 < z < 2.5$ are more modest than what is suggested based solely on the 24 μm flux densities.

Under the assumption that dust heating from star formation powers the IR luminosities, the 24 μm–derived SFRs for many sources are $\gtrsim 1000\ M_\odot\ yr^{-1}$, even after excluding X-ray and IR–power-law sources. Such systems are not observed locally, even in *IRAS*-selected samples (e.g., Sanders et al. 1991; Kennicutt 1998). Including the average 70 and 160 μm flux densities from our stacking analysis reduces the implied SFRs for bright 24 μm sources at $1.5 < z < 2.5$ substantially, such that the vast majority of sources have $\Psi < 1000\ M_\odot\ yr^{-1}$ (see Fig. 11). Indeed, sources with $\Psi > 1000\ M_\odot\ yr^{-1}$ are very rare, with a surface density of $30 \pm 10\ deg^{-2}$, corresponding to $2 \pm 1 \times 10^{-6}\ Mpc^{-3}$ over $1.5 < z < 2.5$, and consistent with the space density of submillimeter galaxies with comparable luminosities (Chapman et al. 2005). Locally, *IRAS*–selected ULIRGs with SFRs of many hundred solar masses per year have large gas masses, $M(H_2) \sim 10^{11}\ M_\odot$,

[10] We note that the SK07 AGN models may not underestimate the total IR luminosity as there are few extreme SK07 models where the expected 24 μm flux density at $z = 2$ (for a given L_{IR}) is higher for star-forming regions than for AGNs, see Fig. 6.

within small, centrally concentrated radii, $r \lesssim 2$ kpc (see Kennicutt 1998). These galaxies represent cases of a near-maximal rate of star formation under physical and dynamical arguments, which convert all their gas into stars in one dynamical time (e.g., Lenhert & Heckman 1996). Current measurements of the gas masses at high redshifts are limited to radio galaxies, but show that large gas reservoirs abound (e.g., Greve et al. 2004). Many distant star-forming galaxies have small rest-frame optical sizes (Trujillo et al. 2004; Papovich et al. 2005), comparable to the IR-emitting regions in local ULIRGs, and such conditions may exist in $z \sim 2$ galaxies with these high SFRs. However, there are star-forming galaxies at $z \sim 2$ with extended sizes ($R \gtrsim 4$ kpc) (Labbé et al. 2003; Zirm et al. 2007), and clearly it is important to measure the range of sizes of high-redshift IR-luminous galaxies directly. Nevertheless, because the majority of high-redshift galaxies in our 24 μm–selected sample have $\lesssim$1000 $M_{\odot}$ yr^{-1}, these galaxies may have similar feedback and star formation efficiencies comparable as lower redshift analogs.

Although local systems with star formation of this magnitude are relatively rare, they are $\approx$1000 times more common at $z \approx 2$ (Daddi et al. 2005; Papovich et al. 2006). As noted by Daddi et al. (2005, see also 2007a), the high 24 μm–detection fraction of galaxies at $1.5 < z < 2.5$ implies that if the IR–active phases are short-lived (on the order of a dynamical time) they must undergo a high duty cycle. Thus, if a high-redshift starburst consumes the available gas mass, there must be an accompanying mechanism to replenish the galaxies' gas supply and drive it to high densities (e.g., cold-gas flows or successive galaxy mergers), in order to maintain the high detection fraction. Logically, the reservoir of molecular gas in galaxies is substantially higher at $1.5 < z < 2.5$ than at present, and the enhanced fraction of systems with maximal SFRs is likely a consequence of the fact that more gas is available to fuel starbursts or AGNs. Thus, it may also be the case that the lower number density of these systems at present is a consequence of the fact that gas required to fuel IR-luminous stages of galaxy evolution occurs with less frequency.

5. CONCLUSIONS

In this paper we explored the *Spitzer* 24, 70, and 160 μm properties of high-redshift galaxies. Our primary interest is to improve the constraints on the total infrared (IR) luminosities of these galaxies. We studied the 24–160 μm flux densities of galaxies as a function of IR and X-ray activity using a K_s-band–selected sample of galaxies from the MUSYC data in the ECDF-S. From $z \approx 0$ to 1.5, the majority of galaxies detected at 70 and 160 μm have flux density ratios consistent with local star-forming galaxies and AGN. Only four galaxies at $1.5 < z < 2.5$ are detected at 70 μm to the depth of the MIPS data (>4.6 mJy, 3 σ at 70 μm), and these have high S_{70}/S_{24} flux density ratios.

There are no galaxies with $1.5 < z < 2.5$, high 24 μm flux densities ($S_{24} > 0.6$ mJy) detected directly at 70 μm or 160 μm. Bright 24 μm sources therefore have low 70 μm flux densities, $S_{70} < 4.6$ mJy. This is not expected if these bright 24 μm sources have SEDs consistent with expectations from empirical templates of local star-forming IR-luminous galaxies. While some bright 24 μm sources at these redshifts and flux densities with published mid-IR spectra have strong PAH emission features, most have featureless spectra. Therefore, the low S_{70}/S_{24} ratios are not due solely to boosted 24 μm from PAHs. It is more likely that their S_{70}/S_{24} ratios result from warm dust temperatures.

Because so few 24 μm sources at $1.5 < z < 2.5$ are detected directly in the longer wavelength *Spitzer* data, we used a stacking analysis to study the average 70 and 160 μm flux density of sources at this redshift as a function of 24 μm flux density, X-ray activity, and rest-frame near-IR color.

Ordinary IR sources at $1.5 < z < 2.5$ with $53 < S_{24}/\mu\text{Jy} < 100$ and $100 < S_{24}/\mu\text{Jy} \leq 250$ have average flux densities $S_{70} = 0.88$ and 1.5 mJy, respectively. The average flux densities at 160 μm are 4.6 and 5.1 mJy, respectively, although these have low S/N ratios (1.8 and 2.3, respectively). For these galaxies the S_{70}/S_{24} ratio and the shape of the observed-frame 24–160 μm SED are generally consistent with empirical models of IR-luminous galaxies. This suggests that *on average* bolometric conversions from the measured 24 μm flux density to total IR luminosities are fair.

Ordinary IR sources at $1.5 < z < 2.5$ with $S_{24} > 250$ μJy have average flux densities of $S_{70} = 2.0$ mJy and $S_{160} = 4.6$ mJy. These sources have average S_{70}/S_{24} ratios substantially lower than predicted from our empirical models of local star-forming galaxies, although they are similar to the local ULIRG IRAS 08572+3915 (Armus et al. 2007). Theoretical model fits to the average 24, 70, and 160 μm flux densities have compact star-forming regions with warm dust temperatures. Such conditions may be expected theoretically as high-redshift galaxies with high gas densities and small sizes similar to local ULIRGs should have high dust temperatures (Kaviani et al. 2003). Observationally, many star-forming galaxies at high-redshifts have small optical sizes comparable to the IR-emitting regions of local ULIRGs (Trujillo et al. 2004; Papovich et al. 2005), and we expect the IR-emitting region to be no bigger than the optical radius. Thus, if star formation powers high-redshift sources with $S_{24} > 250$ μJy, these objects generally are compact with warm dust temperatures. Deep high-angular resolution imaging of these sources either at rest-frame optical wavelengths (e.g., with *HST*) or in the far-IR (ALMA) are needed to measure the size distribution of these sources. Alternatively, ordinary IR sources with $S_{24} > 250$ μJy at $1.5 < z < 2.5$ have S_{70}/S_{24} ratios comparable to X-ray sources with similar 24 μm flux densities. The S_{70}/S_{24} ratios for these sources are also similar to the red tail of QSOs distribution (Elvis et al. 1994). Therefore, there may be a significant AGN contribution to the mid-IR colors of these galaxies. Theoretical model fits to the average 24, 70, and 160 μm flux densities shows they are consistent with dust heating from star formation or AGN. Moreover, they may also involve AGN/starburst composites.

We compared the total IR luminosities for $1.5 < z < 2.5$ galaxies derived from the average 24, 70, and 160 μm flux densities and those inferred solely from the 24 μm data. For ordinary IR sources and $53 < S_{24}/\mu\text{Jy} < 100$ or $100 < S_{24}/\mu\text{Jy} < 250$, the $L_{\rm IR}$(24, 70, 160 μm) values are within factors of $\approx$2–3 of $L_{\rm IR}$(24 μm) (with a dependency on redshift and on the choice of empirical or theoretical model). However, ordinary IR sources and $S_{24} > 250$ μJy have larger ratios of $L_{\rm IR}$(24 μm)/$L_{\rm IR}$(24, 70, 160 μm) ranging from factors of $\approx$3–10 (again depending on redshift and the choice of model). X-ray and IR–power-law sources have fairly substantial ratios, ranging from factors of 2 to $\approx$10. In all cases, the IR luminosities derived solely from the 24 μm data for bright sources, $S_{24} > 250$ μJy are overestimated, in some cases by large factors.

We investigated how the average 70 and 160 μm flux densities affects the interpretation of the bolometric luminosities and SFRs in galaxy samples at $1.5 < z < 2.5$ in the MUSYC data. Using the bolometric luminosities derived using the measured 24 μm flux densities, with the average 70, and 160 μm flux densities, the majority of 24 μm–selected galaxies at $1.5 < z_{\rm ph} < 2.5$ have IR luminosities $L_{\rm IR} \lesssim 6 \times 10^{12}$ $L_{\odot}$, which, if attributed to star formation, corresponds to $\lesssim$1000 $M_{\odot}$ yr^{-1}. This is similar to the maximal star formation rate observed in low-redshift galaxies,

suggesting that high-redshift galaxies may have similar star formation efficiencies and feedback processes. Objects with $L_{IR} > 6 \times 10^{12}\ L_{\odot}$ are quite rare, with a surface density $\sim 30 \pm 10\ \mathrm{deg}^{-2}$, corresponding to $\sim 2 \pm 1 \times 10^{-6}\ \mathrm{Mpc}^{-3}$ over $1.5 < z < 2.5$.

We wish to thank our collaborators on the MUSYC and MIPS GTO teams for many interesting discussions, and for their much hard work. We also thank the anonymous referee for their suggestions, which improved the quality and clarity of this paper. This work is also based in part on data obtained with the *Spitzer Space Telescope*, which is operated by the Jet Propulsion Laboratory (JPL), California Institute of Technology (Caltech) under a contract with NASA. Support for this work was provided by NASA through the *Spitzer Space Telescope* Fellowship Program, through a contract issued by JPL, Caltech under a contract with NASA.

APPENDIX A

STACKING *SPITZER* MIPS DATA

The vast majority of *Spitzer*/MIPS 24 μm sources with $1.5 < z < 2.5$ are undetected to the flux density limits of the MIPS 70 and 160 μm data. To study the far-IR properties of these sources, we resort to stacking the 70 and 160 μm data at the positions of the 24 μm

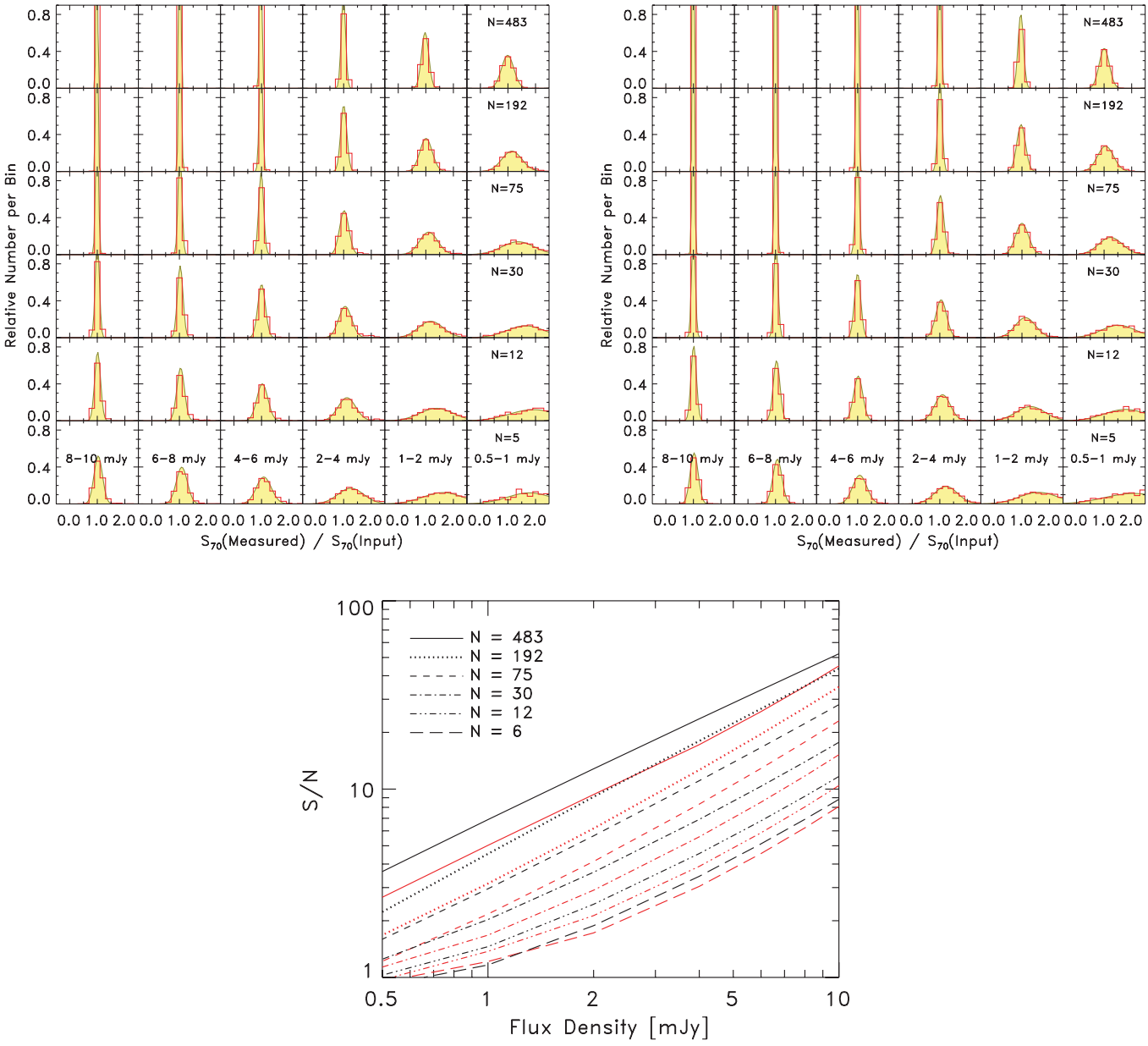

FIG. 12.—Top panels show the distribution of recovered 70 μm flux densities from stacking simulations. Each subpanel shows the distribution of the ratio of measured 70 μm flux density to input flux density. Each column shows this distribution as a function of measured 70 μm flux density (as labeled), and each row shows this distribution as a function of the number of sources in the stack, N (as labeled). The left top panel shows the results from stacking sources in the original image containing all 70 μm sources. The right top panel shows the results from stacking sources in images that have had sources detected at 70 μm with >5 σ significance removed. The bottom panel shows the S/N for the simulated stacked images as a function of flux density, where we derive the S/N using the width of the distributions as an estimate of the flux density error. The line types show the S/N as a function of N objects in each stack, as labeled in the figure inset. Black lines correspond to stacked images that have had bright sources removed. Red lines correspond to stacked images without removing sources.

sources. Several studies have illustrated the benefit of stacking sources in MIPS data (Zheng et al. 2006, 2007; Dole et al. 2006; Huynh et al. 2007; Dye et al. 2007). In this section we describe our stacking methodology, adapted from these prior works.

The first step in the stacking procedure is to take a small subimage from the 70 and 160 μm data centered at the astrometric position of each 24 μm source to be stacked. For this step, we use subimages of approximately $200'' \times 200''$ for both the 70 and 160 μm data. The subimage size does not affect the average (stacked) value so long as it encompasses sufficient area for a local background measurement to be made on the stacked source. We use a two-dimensional bilinear interpolation to center the 70 and 160 μm subimages on the astrometric coordinates of the 24 μm source. We then subtract the local background measured in annuli of $39''$–$65''$ and $32''$–$56''$ of each 70 and 160 μm subimage, respectively.

In the second step we sum the images and take the mean to derive the average flux density of the sample. Following Dole et al. (2006) and Huynh et al. (2007), we rotate each subimage by 90° relative to the previous subimage to reduce the effects of image artifacts on the average measurement. We experimented using other combination schemes, including taking the median of each pixel in the stack or taking the mean after rejecting outliers. In general, we found these to all be consistent once we removed sources detected in the 70 and 160 μm (see below). Thus, the method used to combine the subimages is secondary relative to ensuring that the subimages are clean of bright sources.

We tested our stacking method using simulations of artificial sources of known flux density randomly placed in the ECDF-S 70 and 160 μm images. We compared the accuracy of the flux density measured in the stacked image to the true value. We performed 10,000 Monte Carlo simulations for each bin of flux density and number of objects to measure reliable statistics as a function of flux density and number of objects in the stack. Figure 12 shows the distribution of the ratio of the measured flux density to the true (input) flux density as a function of flux density and number of sources for the 70 μm simulations. The width of the distribution increases with decreasing 70 μm flux density, and decreasing number of objects each stack. We find similar behavior in the distribution for the 160 μm simulations.

The mean of the measured-to-input flux density ratio shifts to values greater than one for low numbers of objects and fainter flux density. This is a consequence of two effects. One is that the flux from nearby detected objects bias the measured flux density. The other is a result of "confusion noise" from nearby unresolved sources, which contribute to the average stacked value (and similar to the effect in confusion-limited submillimeter photometry discussed by Coppin et al. 2005). To suppress the effect of detected sources from contributing to the stacking, we repeated our Monte Carlo test after first removing sources with $>5\,\sigma$ detections in the 70 and 160 μm images. The top right panel in Figure 12 shows the distribution of measured-to-input flux values using the source-subtracted images for the 70 μm simulations before stacking.

We found appreciable gains in the accuracy of the average value for images cleaned of sources detected in the 70 and 160 μm images. We derive the error, σ, on the stacking measurement using the width of the distribution of measured-to-input flux ratio. The bottom panel of Figure 12 illustrates the gain in S/N ($=f_\nu/\sigma$) measured from the stacked images as a function of flux density and number of objects in each stack. For example, for an average measurement of 100 simulated objects with $S_{70} = 1$ mJy the uncertainty is 0.42 mJy without excluding sources. The uncertainty drops to 0.30 mJy with sources excluded. We therefore use 70 and 160 μm cleaned of sources for our stacking analysis.

REFERENCES

Alexander, D. M., Smail, I., Bauer, F. E., Chapman, S. C., Blain, A. W., Brandt, W. N., & Ivison, R. J. 2005, Nature, 434, 738
Alexander, D. M., et al. 2003, AJ, 126, 539
Alonso-Herrero, A., Rieke, G. H., Rieke, M. J., Colina, L., Pérez-González, P. G., & Ryder, S. D. 2006a, ApJ, 650, 835
Alonso-Herrero, A., et al. 2006b, ApJ, 640, 167
Armus, L., et al. 2007, ApJ, 656, 148
Bell, E. F. 2003, ApJ, 586, 794
Bell, E. F., et al. 2005, ApJ, 625, 23
Bertin, E., & Arnouts, S. 1996, A&AS, 117, 393
Brandl, B. R., et al. 2006, ApJ, 653, 1129
Calzetti, D., et al. 2005, ApJ, 633, 871
———. 2007, ApJ, 666, 870
Caputi, K. I., et al. 2006, ApJ, 637, 727
Chanial, P., Flores, H., Guiderdoni, B., Elbaz, D., Hammer, F., & Vigroux, L. 2007, A&A, 462, 81
Chary, R. R., & Elbaz, D. 2001, ApJ, 556, 562 (CE01)
Chapman, S. C., Blain, A. W., Smail, I., & Ivison, R. J. 2005, ApJ, 622, 772
Chapman, S. C., Helou, G., Lewis, G. F., & Dale, D. A. 2003a, ApJ, 588, 186
Coppin, K., Halpern, M., Scott, D., Borys, C., & Chapman, S. 2005, MNRAS, 357, 1022
Daddi, E., et al. 2005, ApJ, 631, L13
———. 2007a, ApJ, in press (arXiv: 0705.2831)
———. 2007b, ApJ, in press (arXiv: 0705.2832)
Dale, D. A., & Helou, G. 2002, ApJ, 576, 159 (DH02)
Dale, D. A., Helou, G., Contursi, A., Silbermann, N. A., & Kolhatkar, S. 2001, ApJ, 549, 215
Dale, D. A., et al. 2005, ApJ, 633, 857
De Lucia, G., Springel, V., White, S. D. M., Croton, D., & Kauffmann, G. K. 2006, MNRAS, 366, 499
Devriendt, J. E. G., Guiderdoni, B., & Sadat, R. 1999, A&A, 350, 381
Dickinson, M., Papovich, C., Ferguson, H. C., & Budavári, T. 2003, ApJ, 587, 25
Dole, H., et al. 2004, ApJS, 154, 87
———. 2006, A&A, 451, 417
Donley, J. L., Rieke, G. H., Pérez-González, P. G., Rigby, J. R., & Alonso-Herrero, A. 2007, ApJ, 660, 167
Dye, S., Eales, S. A., Ashby, M. L. N., Huang, J.-S., Egami, E., Brodwin, M., Lilly, S., & Webb, T. 2007, MNRAS, 375, 725
Egami, E., et al. 2004, ApJS, 154, 130
Elbaz, D., Cesarsky, C. J., Chanial, P., Aussel, H., Franceschini, A., Fadda, D., & Chary, R. R. 2002, A&A, 384, 848
Elbaz, D., et al. 1999, A&A, 351, L37
Elvis, M., et al. 1994, ApJS, 95, 1
Fontana, A., et al. 2003, ApJ, 594, L9
———. 2004, A&A, 424, 23
Franceschini, A., Aussel, H., Cesarsky, C. J., Elbaz, D., & Fadda, D. 2001, A&A, 378, 1
Frayer, D. T., Armus, L., Scoville, N. Z., Blain, A. W., Reddy, N. A., Ivison, R. J., & Smail, I. 2003, AJ, 126, 73
Frayer, D. T., et al. 2006a, AJ, 131, 250
———. 2006b, ApJ, 647, L9
Gawiser, E., et al. 2006, ApJS, 162, 1
Giacconi, R., et al. 2002, ApJS, 139, 369
Glazebrook, K., et al. 2004, Nature, 430, 181
Gordon, K., et al. 2005, PASP, 117, 503
Greve, T. R., Ivison, R. J., & Papadopoulos, P. P. 2004, A&A, 419, 99
Hogg, D. W. 2001, AJ, 121, 1207
Houck, J. R., et al. 2005, ApJ, 622, L105
Huynh, M. T., Pope, A., Frayer, D. T., & Scott, D. 2007, ApJ, 659, 305
Kaviani, A., Haehnelt, M. G., & Kauffmann, G. 2003, MNRAS, 340, 739
Kennicutt, R. C. 1998, ARA&A, 36, 189
Labbé, I., et al. 2003, AJ, 125, 1107
Lacy, M., et al. 2004, ApJS, 154, 166
Lagache, G., Dole, H., & Puget, J.-L. 2003, MNRAS, 338, 555
Le Floc'h, E., et al. 2005, ApJ, 632, 169
———. 2007, ApJ, 660, L65
Lehmer, B. D., et al. 2005, ApJS, 161, 21
Lenhert, M. D., & Heckman, T. M. 1996, ApJ, 472, 546
Maraston, C., Daddi, E., Renzini, A., Cimatti, A., Dickinson, M., Papovich, C., Pasquali, A., & Pirzkal, N. 2006, ApJ, 652, 85
Marcillac, D., Elbaz, D., Chary, R. R., Dickinson, M., Galliano, F., & Morrison, G. 2006, A&A, 451, 57

McCarthy, P. J. 2004, ARA&A, 42, 477
Papovich, C., & Bell, E. F. 2002, ApJ, 579, L1
Papovich, C., Dickinson, M., Giavalisco, M., Conselice, C. J., & Ferguson, H. C. 2005, ApJ, 631, 101
Papovich, C., et al. 2004, ApJS, 154, 70
———. 2006, ApJ, 640, 92
Pérez-González, P. G., et al. 2005, ApJ, 630, 82
Pope, A., et al. 2006, MNRAS, 370, 1185
Reddy, N. A., Steidel, C. C., Fadda, D., Yan, L., Pettini, M., Shapley, A. E., Erb, D. K., & Adelberger, K. L. 2006, ApJ, 644, 792
Renzini, A. 2006, ARA&A, 44, 141
Rieke, G., et al. 2004, ApJS, 154, 25
Rigby. J. R., et al. 2007, ApJ, submitted
Roussel, H., Sauvage, M., Vigroux, L., & Bosma, A. 2001, A&A, 372, 427
Rowan-Robinson, M. 2001, ApJ, 549, 745
Rudnick, G., et al. 2001, AJ, 122, 2205
———. 2003, ApJ, 599, 847
———. 2006, ApJ, 650, 624
Sajina, A, Yan, L., Armus, L., Choi, P., Fadda, D., Helou, G., & Spoon, H., 2007, ApJ, 664, 713
Sanders, D. Scoville, N., & Soifer, B. T. 1991, ApJ, 370, 158
Siebenmorgen, R., & Krügel, E. 2007, A&A, 461, 445 (SK07)
Silva, L., Granato, G. L., Bressan, A., & Danese, L. 1998, ApJ, 509, 103
Smith, J. D. T., et al. 2007, ApJ, 656, 770
Soifer, B. T., & Neugebauer, G. 1991, AJ, 101, 354
Soifer, B. T., Neugebauer, G., & Houck, J. R. 1987, ARA&A, 25, 187
Stern, D., et al. 2005, ApJ, 631, 163
Teplitz, H., et al. 2007, ApJ, 659, 941
Trujillo, I., et al. 2004, ApJ, 604, 521
van der Wel, A., Franx, M., Wuyts, S., van Dokkum, P. G., Huang, J., Rix, H.-W., & Illingworth, G. D. 2006, ApJ, 652, 97
van Dokkum, P. G., et al. 2006, ApJ, 638, L59
Virani, S. N., Treister, E., Urry, C. M., & Gawiser, E. 2006, AJ, 131, 2373
Wang, B., & Heckman, T. M. 1996, ApJ, 457, 645
Webb, T. M. A., et al. 2006, ApJ, 636, L17
Weedman, D. W., Le Floc'h, E., Higdon, S. J. U., Higdon, J. L., & Houck, J. R. 2006a, ApJ, 638, 613
Weedman, D. W., et al. 2006b, ApJ, 651, 101
Yan, L., et al. 2005, ApJ, 628, 604
———. 2007, ApJ, 658, 778
Zheng, X. Z., Bell, E. F., Rix, H.-W., Papovich, C., Le Floc'h, E., Rieke, G. H., & Pérez-González, P. G. 2006, ApJ, 640, 784
Zheng, X. Z., Dole, H., Bell, E. F., Le Floc'h, E., Rieke, G. H., Rix, H.-W., & Schiminovich, D. 2007, ApJ, in press (arXiv: 0706.0003)
Zirm, A. W, et al. 2007, ApJ, 656, 66